Multiuser-MISO Precoding Under Channel Phase Uncertainty in Satellite Communication Systems

LIZ MARTINEZ MARRERO [1] **(Student Member, IEEE), ALIREZA HAQIQATNEJAD** [2] **(Member, IEEE),**
JUAN C. MERLANO DUNCAN [1] **(Senior Member, IEEE), SYMEON CHATZINOTAS** [1] **(Senior Member, IEEE),**
AND BJÖRN OTTERSTEN [1] **(Fellow, IEEE)**

[1]Interdisciplinary Centre for Security, Reliability and Trust (SnT), University of Luxembourg, 1855 Luxembourg City, Luxembourg
[2]OQ Technology, 3364 Leudelange, Luxembourg

CORRESPONDING AUTHOR: LIZ MARTINEZ MARRERO (e-mail: liz.martinez-marrero@uni.lu)

ABSTRACT Linear and symbol-level precoding in satellite communications have received increasing research attention thanks to their ability to tackle inter-beam interference, allowing the use of spectral resources more efficiently. However, there are still challenges and open questions regarding the implementation of practical precoding systems taking the phase uncertainties in estimating the channel state information into account. This work assesses the impact of phase variations and uncertainties inherent to the satellite communication system operating a precoded forward link. Specifically, we address the inability to measure at the user terminal, the absolute phase rotation introduced by the channel, and the transponder local oscillator phase noise effects on the precoding operations considering the use of frequency division multiplexing in the forward-uplink transmission. We formally demonstrate that the system performance for linear and non-linear precoding operations is not affected by the uncertainty in the phase measurements at the user terminal. Additionally, we show that using a single frequency reference for all the local oscillators at the transponder does not avoid the phase variations related to the frequency division multiplexing in the forward-uplink. This work demonstrates that these phase variations would not affect the system performance for an ideal zero-delay precoding loop. However, this is not feasible in practical scenarios, where the phase noise of the frequency reference at the transponder and the loop delay determine the impact on the system performance. We validate our results by simulations considering three frequency references with different stability levels in a typical geosynchronous orbit (GEO) satellite system. Our results suggest that practical implementations of multiuser-MISO precoding systems must include a differential phase synchronization loop to compensate for this performance degradation.

INDEX TERMS Linear precoding, multiuser-MISO precoding, phase uncertainties, satellite communication system, symbol level precoding, system performance.

I. INTRODUCTION

Multi-user multiple-input single-output MU-MISO precoding has been studied in several telecommunication areas to compensate for multi-user interference (MUI), allowing more aggressive frequency reuse. Several examples of this trend are present in the latest WiFi [1], multiple input multiple output (MIMO) power line communications [2], and 5G New Radio [3].

In this context, linear precoding approaches have been increasingly popular in recent years as an appealing method of mitigating MUI while ensuring specific service requirements. In particular, precoding techniques proved to be effective

against MUI for multibeam satellite communications [4], [5].

Broadband data services have become a driver for satellite systems, and precoding technology has received much attention as it can significantly increase the spectral efficiency of multibeam systems. It became a natural consequence of the evolution of satellite systems to provide broadband services despite the scarcity of spectral resources [6], [7].

The research community has been extensively studying the linear precoding design problem. The main research directions include the extension of precoding to multicast scenarios [8], making it more robust to payload imperfections, including non-linearities and distortions [9], [10], and making it robust to imperfections in the channel state information (CSI) estimation [11].

Moreover, precoding is now supported through dedicated framing and signaling in the latest Extension of the Digital Video Broadcasting - Satellite Second Generation (DVB-S2X) standard; see in particular [12]. The industry has also shown interest, corroborated by a live demonstration of precoding over the satellite [5]. Some more sophisticated techniques propose advanced non-linear precoding methods. In such methods, the output of the precoding operation is a non-linear operation combining the vector of input data symbols and the CSI, laying the foundation for what is known as symbol-level precoding (SLP) [13]. SLP technique is a promising approach that can achieve additional gains compared to the linear channel inversion methods at the cost of additional computational complexity [14], [15]. In many cases, the additional complexity of the proposed algorithms is prohibitive for practical systems. However, many computationally efficient techniques have been proposed in the literature to make SLP feasible under realistic scenarios; see, for example, [16], [17], [18], [19], [20].

Despite the increasing interest in standardizing precoding use in multibeam satellite systems, of which the latest DVB-S2X standard [12] is an example; there are not many precoding over satellite examples, mainly due to the strict synchronization requirements for both linear [4], [5] and symbol level [16], [17] precoding implementations. Some authors mention this problem as part of precoding designs, proposing a general solution without a detailed analysis of the synchronization impairments [4], [5].

Specifically for GEO stationary multibeam satellite systems, the synchronization problem is addressed considering that all the beams are generated using a single frequency reference at the satellite transponder [12], [21], [22]. However, practical transponders avoid transmitting all their beams with a single frequency reference for scalability, reliability, and security reasons, among others. The synchronization impairments are even worse for distributed satellite systems [4], where it is impossible to use a common frequency reference for different spacecraft, and for non-geostationary orbit (NGSO) satellites, where the Doppler effect produces phase distortions. As we will demonstrate in the next sessions, even for the best synchronization scenario, with all the beams

generated using a single frequency reference, the performance of precoding implementations is affected by synchronization impairments inherent to the satellite communication systems.

Some authors have analyzed in detail the impact of the implementation's phase uncertainties and the channel estimation errors on precoding performance for Massive MIMO systems. For instance, [23] studied the performance of linear precoding techniques in Massive MIMO systems considering memoryless non-linear distortions at the transmitter side (high power amplifier (HPA), as an example) and imperfect CSI estimation. In this work, the authors approximated the precoded signal by a complex Gaussian distribution. This assumption only applies to Massive MIMO systems, where the precoding matrix has large dimensions. Similarly, [24] studies the impact of the phase noise of free-running oscillators on the performance of linear Massive MIMO precoding systems. Meanwhile, [25] compared two linear precoding techniques for a Massive MIMO system considering channel non-reciprocity and errors in the CSI estimation. In addition, other authors assessed the performance of Massive MIMO linear [26] and non-linear [27] precoding techniques but without considering any of the synchronization impairments previously mentioned. None of these works deal with satellite communication systems but terrestrial mobile communications. The communication channel is different for precoding-enabled terrestrial and satellite communications. While the user terminals (UTs) and the base station (BS), where the precoding is calculated, share a direct link in mobile communications, in satellite systems, the precoding is calculated at the gateway (GW), which transmits the precoded data streams to the satellite using frequency division multiplexing (FDM) and the satellite transponder generates the precoded beams towards the UTs.

Other authors have studied the performance of linear [22], [28], and non-linear [21] precoding in satellite communication systems. However, most of them limit the analysis to including synchronization impairments in their simulations without any formal demonstrations [21], [22]. In [21], the authors point out that the channel slow time variations can be followed by the receiver as long as they are equal to all the beams. Leading to the recommendation of using a common reference for all the onboard oscillators [21]. Meanwhile, the simulations results presented in [22] suggested that linear precoding techniques such as zero-forcing (ZF) and minimum mean square error (MMSE) can compensate for the receivers' signal-to-noise-plus-interference ratio (SNIR) degradation related to the use of multiple onboard oscillators.

Therefore, it is evident the need for a formal analysis considering the effects of the synchronization impairments over the performance of precoding-enabled satellite systems. Based on the previous works [21], [22], and considering the characteristics of satellite communication systems, where the precoding is calculated at the GW and generated at the satellite transponder, it is advisable to analyse independently the impact on the uplink (from GW to satellite) and the downlink (from satellite to UTs) channels. Consequently, we propose

a model in which we decompose the entire channel matrix into three different matrices that are the factorization of the entire one. Two of those three matrices are the forward uplink and downlink phase-uncertainty matrices, respectively. This methodology lays the foundations for designing the different components of an end-to-end satellite system using the precoding technique, such as the CSI estimation, the precoding matrix computation, and the precoding application.

This work aims at assessing the impact of the phase errors and uncertainties in operating a precoded forward link satellite communication system. It formally demonstrates that the phase uncertainties created in the forward-downlink do not affect the precoding performances for linear precoding operation. Then, we also confirm this fact for the case of non-linear precoding systems. Additionally, this paper shows that the UTs estimate the phase variations added in the forward-uplink channel as part of the CSI. We confirm our analytical findings by employing computer simulations for different system configurations. We consider three different phase noise level profiles for the transponder frequency reference in a typical end-to-end GEO satellite system in these simulations. It is essential to clarify that during this work, we name frequency reference to the crystal oscillator used as a reference for one or more local oscilators (LOs). For the sake of simplicity, we will assume that all the LOs at the transponder have a common frequency reference for our simulations. Finally, this paper suggests alternatives to be explored in future non-linear precoding techniques under the aforementioned phase variations and phase uncertainties seen in the forward link of a multibeam satellite channel.

In short, the main contributions of this article are the following:

- Identification of the individual contribution of each element of the system to the overall synchronization uncertainties in practical precoding implementations. This allows for more efficient designs and implementations.
- Formal demonstration for linear and non-linear precoding, that the UTs can track slow time variations in the channel as long as they equally affect all the beams, as it was suggested but not demonstrated in [21] for non-linear precoding.
- Formal demonstration that the uplink phase variations related to the Doppler effect and the multiple LOs required at the transponder affect precoding performance even when all the LOs share a single frequency reference. This paper demonstrates that these uplink phase variations will not affect the system performance for an ideal loop with a negligible delay between the CSI estimation and the precoding matrix application. However, since the zero-delay loop is unfeasible in actual systems, this article demonstrates that practical implementations of precoding require an extra synchronization solution as much for a single frequency reference as for multiple frequency references. Previous works assumed that using a single frequency reference was enough for multibeam satellite systems [21], [22].

- Comparison of the robustness to synchronization impairments of MMSE, ZF, and SLP techniques.

The rest of this paper is organized as follows. Section II presents the system model, and Section III provides a detailed analysis of the phase errors and uncertainties sources in a precoding satellite system. Section IV discusses the effects of the absolute phase uncertainty in linear and non-linear precoding methods. The effects of the phase variations in the forward-uplink channel for linear precoding methods are also analyzed in IV. Section V focuses on robust designs considering the phase impairment seen in practical implementations, and Section VI presents some simulation results to validate the analytical discussion. Finally, conclusions regarding the impact of this work and future directions on the design of precoding satellite systems are provided in Section VII.

A. NOTATIONS

We use uppercase and lowercase bold-faced letters to denote matrices and vectors, respectively. The sets of real and complex numbers are represented by $\mathbb{R}$ and $\mathbb{C}$. For a matrix $\mathbf{A}$, $\mathcal{R}(\mathbf{A})$ represents the column space of $\mathbf{A}$. diag($\cdot$), or blkdiag($\cdot$), represents a square (block) matrix having main-diagonal (block) entries and zero off-diagonals. For a set S, |S| denotes the cardinality of S. Given two vectors $\mathbf{x}$ and $\mathbf{y}$ with equal dimensions, $\mathbf{x} \succeq \mathbf{y}$ (or $\mathbf{x} \succ \mathbf{y}$) denotes the entrywise inequality. $\| \cdot \|_2$ represent the vector Euclidean norm. $\mathbf{I}$ and $\mathbf{0}$ respectively stand for the identity matrix and the zero-matrix (or the zero vector, depending on the context) of appropriate dimensions. The operator $\otimes$ stands for the Kronecker product.

B. LIST OF ACRONYMS

AWGN	additive white Gaussian noise.
BS	base station.
CI	constructive interference.
CIR	constructive interference region.
CSI	channel state information.
DVB-S2X	Extension of the Digital Video Broadcasting - Satellite Second Generation.
FDM	frequency division multiplexing.
GEO	geosynchronous orbit.
GW	gateway.
HPA	high power amplifier.
LO	local ocilator.
MIMO	multiple input multiple output.
MMSE	minimum mean square error.
MU-MISO	multi-user multiple-input singleoutput.
MUI	multi-user interference.
NGSO	non-geostationary orbit.
NNLS	non-negative least squares.
PLL	phase-locked loop.
PN	phase noise.
PSD	power spectral density.
QoS	quality of service.
SER	symbol error rate.
SLP	symbol-level precoding.
SNIR	signal-to-noise-plus-interference ratio.

SNR   signal-to-noise ratio.
UT   user terminal.
ZF   zero-forcing.

II. SYSTEM MODEL

We consider a wireless multi-antenna downlink system where the transmitter, equipped with N antennas, serves K ($K \leq N$) single-antenna UTs by sending K spatially-multiplexed (i.e., precoded) independent data streams. We collect in $\mathbf{h}_k \in \mathbb{C}^{N \times 1}$ the complex (i.e., magnitude plus phase) coefficients of the frequency-flat slow fading channels between the transmitter's antennas and the kth UT. At a given symbol period, independent data symbols $\{s_k\}_{k=1}^{K}$ are to be transmitted to the UTs, where s_k denotes the symbol intended for the kth user. Under the above assumptions, the received vector containing the symbol-sampled complex baseband received signals of all K UTs can be modelled as

$$\mathbf{r} = \mathbf{HWs} + \mathbf{z}, \tag{1}$$

where $\mathbf{H} = [\mathbf{h}_1, \ldots, \mathbf{h}_K]^T$ denotes the $K \times N$ complex-valued channel matrix, $\mathbf{W}$ stands for the $N \times K$ precoding matrix, $\mathbf{s} = [s_1, s_2, \ldots, s_K]^T$ is a $K \times 1$ complex-valued vector containing the UTs' intended modulated symbols, and $\mathbf{z}$ collects independent additive noise components at the UTs' receivers, which are modeled as circularly symmetric complex Gaussian (CSCG) random variables with zero mean and variance σ^2.

The physical channel matrix collecting the complex channel coefficients for all K UTs can be written as

$$\mathbf{H} = \begin{bmatrix} |h_{11}|e^{j\psi_{11}} & |h_{12}|e^{j\psi_{12}} & \cdots & |h_{1N}|e^{j\psi_{1N}} \\ |h_{21}|e^{j\psi_{21}} & |h_{22}|e^{j\psi_{22}} & \cdots & |h_{2N}|e^{j\psi_{2N}} \\ \vdots & \vdots & & \vdots \\ |h_{K1}|e^{j\psi_{K1}} & |h_{K2}|e^{j\psi_{K2}} & \cdots & |h_{KN}|e^{j\psi_{KN}} \end{bmatrix}, \tag{2}$$

where h_{kj} denotes the channel coefficient between the kth UT and the jth transmit antenna element, for any $k \in \{1, 2, \ldots, K\}$ and $j \in \{1, 2, \ldots, N\}$, and $|h_{k,j}|$ and $\psi_{k,j}$ denote its magnitude and phase, respectively.

It is further assumed that the UTs' intended symbols are taken from an equiprobable constellation set, denoted by $\mathbb{X}$, which is represented in the complex domain as

$$\mathbb{X} = \left\{ x_i \mid x_i \in \mathbb{C}, i = 1, 2, \ldots, M, \frac{1}{M}\sum_{i=1}^{M}|x_i|^2 = 1 \right\}.$$

Accordingly, at any given symbol period, we have $s_k = x_i$ for some $x_i \in \mathbb{X}$. For the brevity of analysis and without loss of generality, we assume identical modulation schemes for all K UTs. The constellation set $\mathbb{X}$ is assumed to be symmetric with respect to (w.r.t.) the origin and has unitary average power. We respectively denote by $\mathbf{bd}(\mathbb{X})$ and $\mathbf{int}(\mathbb{X})$ the sets of boundary and interior points of $\mathbb{X}$, with $|\mathbf{bd}(\mathbb{X})| = M_b$ and $|\mathbf{int}(\mathbb{X})| = M - M_b$. Note that the set of boundary points refers to the symbols that reside on the convex hull of the constellation. We further confine ourselves to constellation sets with uniformly

distributed symbols on $\mathbf{bd}(\mathbb{X})$, e.g., PSK, but we do not make any assumption on the geometry of $\mathbf{int}(\mathbb{X})$.

For our later use in this paper, we define some real-valued notations: $\mathbf{x}_i \triangleq [\text{Re}(x_i), \text{Im}(x_i)]^T$, $\bar{\mathbf{s}}_k \triangleq [\text{Re}(s_k), \text{Im}(s_k)]^T$, $\bar{\mathbf{z}} \triangleq [\mathbf{z}_1, \ldots, \mathbf{z}_k]^T$ with $\bar{\mathbf{z}}_k \triangleq [\text{Re}(z_k), \text{Im}(z_k)]^T$, and $\bar{\mathbf{H}}_k \triangleq \Omega(\mathbf{h}_k)$ where

$$\Omega(\mathbf{y}) \triangleq \begin{bmatrix} \text{Re}(\mathbf{y}) & -\text{Im}(\mathbf{y}) \\ \text{Im}(\mathbf{y}) & \text{Re}(\mathbf{y}) \end{bmatrix},$$

for any complex input vector $\mathbf{y}$.

III. PHASE ERROR SOURCES IN THE FORWARD CHANNEL OF A MU-MISO PRECODING SYSTEM

Typical satellite communication systems consist of a gateway, a satellite transponder, and the UTs [29]. During precoding operations, the gateway calculates the precoding matrix $\mathbf{W}$ and applies it to the UT's intended modulated symbols $\mathbf{s}$. The resulting precoded data streams $\mathbf{u}_j(t)$ with $j \in \{1, \ldots, N\}$ are transmitted to the satellite by FDM using the uplink carrier frequencies f_{u_j}. The transparent satellite transponder simultaneously transmits each data stream to its intended receiver. Traditional multibeam satellite systems divide the bandwidth among the beams, known as four colors reuse. On the other hand, full-frequency reuse approaches, such as precoding, allows the use of the total bandwidth for each beam, which implies that each data stream is converted to the same downlink carrier frequency f_D. Since the precoding matrix $\mathbf{W}$ is calculated as the inverse of the channel $\mathbf{H}$, each UT receives its intended beam without interference ($\mathbf{WH} = \mathbf{I}$, where $\mathbf{I}$ is the Identity matrix). The GW calculates the precoding matrix using the channel estimated at the UTs for each beam. To this end, the GW transmits non-precoded pilots periodically inserted between the precoded payload. The non-precoded pilots contain orthogonal sequences predefined for each beam in such a way that each UT can estimate the channel response for each beam to itself by the correlation of the received signal and the expected signal for that beam. The result of this operation is known as CSI, and it is sent to the GW for the calculation of the following precoding matrix in a continuous closed-loop way. The previous explanation refers to the ideal system; practical implementations present phase errors and uncertainties that impact the final result. This section delves into the phase errors and uncertainties inherent to precoding-enabled satellite systems.

Fig. 1 represents each component's contribution to the system's total phase uncertainty. This work considers an ideal frequency reference at the gateway without phase noise. As explained before, the jth beam uses the uplink carrier frequency f_{U_j}. In addition, we assume the optimal design choice in synchronization terms: to process all the beams at the transponder with a common frequency reference. However, this transponder frequency reference is not ideal, but it presents a phase drift represented as $\phi_0(t)$ in Fig. 3. The phase noise of the transponder frequency reference produces
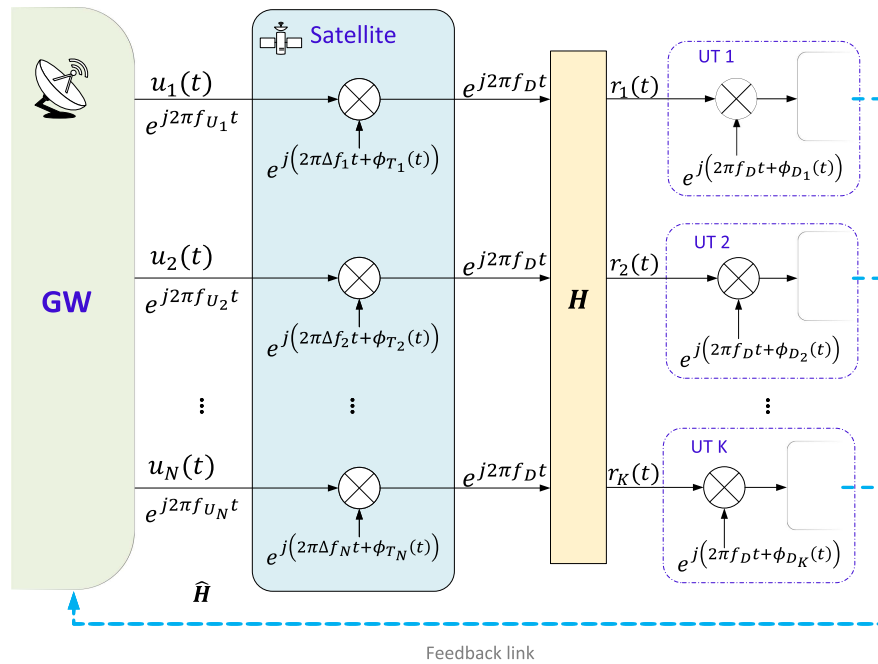
FIGURE 1. Graphical representation of the phase variations and uncertainty sources in a MU-MISO precoding satellite system. In the figure, $u_1(t) \ldots u_N(t)$ are the uplink beams transmitted at carrier frequencies $f_{U_1} \ldots f_{U_N}$ respectively. $\Delta f_1 \ldots \Delta f_1$ represent the different frequencies required to downconvert the uplink signals to the precoding carrier f_D. As mentioned before, $r_1(t) \ldots r_K(t)$ identify the received signal at each UT and terms $\phi_{D_1}(t) \ldots \phi_{D_K}(t)$ represent the phase noise of the LOs at the UTs.
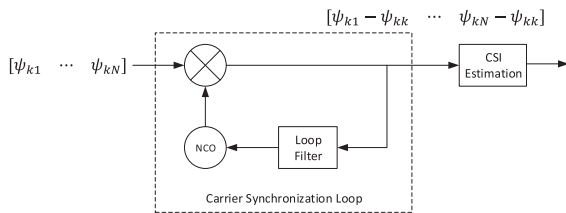

FIGURE 2. Relative phase estimation at the UT due to the carrier synchronization loop.

FIGURE 3. Graphical representation of how the FDM at the uplink and the LOs phase noise affect MU-MISO precoding even when a common frequency reference is used at the transponder.

different phase drifts at the output of each LO. These are represented in Fig. 1 as $\phi_{T_1}(t) \ldots \phi_{T_N}(t)$.

At the downlink channel, all the signals received by the UTs share a common carrier frequency f_D and the phase noise introduced by the LO of the kth UT is represented as $\phi_{D_k}(t)$. For precoding purposes, the CSI estimated by each UT is sent to the gateway through the satellite. In this case, the phase estimations are quantized and digitally transmitted over the return link, and they are protected against channel distortions. For that reason, the feedback channel can be considered ideal. The following subsections will individually analyze the contribution of each system's element to the total phase uncertainty.

A. UNCERTAINTY OF THE PHASE ESTIMATION AT THE UTS' RECEIVERS

Using the non-precoded pilots sent by the GW, a UT acquires its CSI by estimating the magnitudes and the phases of the associated complex channel coefficients. To this end, the non-precoded pilots contain orthogonal sequences specific for each beam. The UT can estimate the CSI from the jth beam to itself as the correlation between the jth orthogonal sequence and the received signal. The UTs estimate the received carrier signal's phase through synchronization loops based on PLLs. Then, all the phase measurements performed by the kth UT are relative to the phase of its intended beam. This implies that the remaining channel phases corresponding to the kth UT are estimated w.r.t. $\hat{\psi}_{k,k}$. More precisely, any $\psi_{k,j}$ with $j \neq k$ is estimated as $\hat{\psi}_{k,j} = \psi_{k,j} - \psi_{k,k}$. On the other hand, we assume that each UT can perfectly estimate the magnitudes of its complex channel coefficients towards the transmitter's antennas.

The phase at the input of the CSI estimator depends on the phase of the received signal $[\psi_{k1} \quad \psi_{kn} \quad \ldots \quad \psi_{kN}]$ and the carrier synchronization loop. This is represented in Fig. 2. After the carrier synchronization loop is locked, its output is $[\psi_{k1} - \psi_{kk} + \phi_{D_k}(t) \quad \psi_{kn} - \psi_{kk} + \phi_{D_k}(t) \quad \ldots \quad \psi_{kN} - \psi_{kk} + \phi_{D_k}(t)]$, where ψ_{kn} and ψ_{kk} are the phase rotation introduced by the channel and ϕ_{D_k} is the phase noise of the frequency reference of the kth UT. The system response of the phase-locked loop (PLL) at the UTs is optimized to minimize the phase noise introduced by the loop $\phi_{D_k}(t)$ [30] in order that $\psi_{kn} - \psi_{kk} >> \phi_{D_k}(t)$ and the phase noise introduced by the UTs can be discarded.

Collecting the estimated channel vectors of all UTs into a matrix form, we can write the measured channel matrix $\hat{\mathbf{H}}_D$ as (4), shown at the bottom of this page, which relates to the physical channel $\mathbf{H}$ as

$$\hat{\mathbf{H}}_D = \boldsymbol{\Psi}_D \mathbf{H}, \tag{3}$$

where $\boldsymbol{\Psi}_D \triangleq \mathrm{diag}(e^{-j\psi_{11}}, e^{-j\psi_{22}}, \ldots, e^{-j\psi_{KK}})$ is referred to as *phase rotation matrix* and contains the absolute phase rotation introduced by the physical channel to each intended beam. These coefficients cannot be measured due to the practical limitations of conventional PLL algorithms.

Each UT feeds its own CSI estimation back to the transmitter. Therefore, only the measured channel matrix $\hat{\mathbf{H}}_D$, and not $\mathbf{H}$, is assumed to be available at the transmitter. The transmitter uses the phase-normalized channel $\hat{\mathbf{H}}_D$ to compute the precoding matrix for the subsequent data transmission towards the UTs.

In what follows, we aim to evaluate the effect of CSI imperfections due to differential phase estimation at the UTs, on the precoding performance. In practice, the phase rotation matrix $\boldsymbol{\Psi}_D$ is unknown at the UTs' receivers. Nonetheless, a pilot-aided phase synchronization loop at the UTs can remove the effect of the phase rotation. We mathematically model this process by assuming that the kth received signal is rotated by the corresponding phase offset ψ_{kk} before detection. We can equally express this operation by multiplying the received signal vector by the rotation matrix $\boldsymbol{\Psi}_D$.

B. PHASE VARIATIONS ADDED DURING THE FREQUENCY DOWN-CONVERSION AT THE TRANSPONDER

Even if a common crystal oscillator is used to process all the beams at the transponder, some phase variations are introduced during the frequency down-conversion. Fig. 3 can be used to illustrate this fact. Considering that all the f_{U_j} with $j \in \{1, 2, \ldots, N\}$ uplink carrier frequencies have to be converted to the same downlink carrier frequency f_D, the transponder has to mix each input with a different single-frequency signal. Using frequency synthesizers can generate different output frequencies from a single reference. However, the phase noise at the output of each LO is determined by the frequency synthesizers in a magnitude proportional to the ratio $\frac{\Delta f_j}{f_0}$ where Δf_j is the synthesized frequency, and f_0 is the nominal frequency of the frequency reference. This implies that the power spectral density (PSD) of the phase noise introduced to the jth beam, $\phi_{T_j}(t)$, is

$$S_{\phi_{T_j}(t)} = S_{\phi_0(t)} + 20 \log_{10}\left(\frac{\Delta f_j}{f_0}\right) \quad \text{(dBc/Hz)}, \tag{5}$$

where $S_{\phi_0(t)}$ is the PSD of the frequency reference phase noise $\phi_0(t)$ at a nominal frequency f_0. The term Δf_j is defined as $\Delta f_j \triangleq f_D - f_{U_j}$ with $j \in \{1, 2, \ldots, N\}$.

Similar to the previous section, we can represent the phase variations introduced to each beam at the transponder as part of the channel estimated at the UTs. In a matrix form,

$$\hat{\mathbf{H}}_U(t) = \mathbf{H}\boldsymbol{\Phi}_U(t), \tag{6}$$

where $\boldsymbol{\Phi}_U(t) \triangleq \mathrm{diag}(e^{j\phi_{T_1}(t)}, e^{j\phi_{T_2}(t)}, \ldots, e^{j\phi_{T_N}(t)})$ is the diagonal matrix containing the phase variations added at the transponder to the jth beam.

Note that (6) does not include the phase estimation uncertainties considered in (3). We address both impairments independently for simplicity in our analysis and without loss of generality.

IV. PRECODING WITH DIFFERENTIAL PHASE ESTIMATION AND PHASE NOISE AT THE TRANSPONDER'S FREQUENCY REFERENCE

In this section, we study different multiuser precoding techniques by assuming that the available CSI used for precoding computation at the transmitter is obtained via a differential phase estimation process described in the previous section. The precoding schemes of interest are the minimum mean squares error (MMSE), as an example of linear precoding techniques, and the optimal distance preserving constructive interference region (DPCIR) based symbol-level precoding.

A. MMSE PRECODING

Given an average total transmit power of p, the MMSE precoder aims to minimize the variance of the difference between the UTs' intended and received symbols. The corresponding optimization problem can be expressed as [31]

$$\min_{\mathbf{W}, \eta} \mathrm{E}\left\{\|\mathbf{s} - \eta^{-1}\mathbf{r}\|^2\right\} \quad \text{s.t.} \quad \mathrm{E}\left\{\|\mathbf{W}\mathbf{s}\|^2\right\} = p, \tag{7}$$

$$\hat{\mathbf{H}}_D = \begin{bmatrix} |h_{11}| & \cdots & |h_{1K}|e^{j(\psi_{1K}-\psi_{11})} & \cdots & |h_{1N}|e^{j(\psi_{1N}-\psi_{11})} \\ |h_{21}|e^{j(\psi_{21}-\psi_{22})} & \cdots & |h_{2K}|e^{j(\psi_{2K}-\psi_{22})} & \cdots & |h_{2N}|e^{j(\psi_{2N}-\psi_{22})} \\ \vdots & \ddots & \vdots & & \vdots \\ |h_{K1}|e^{j(\psi_{K1}-\psi_{KK})} & \cdots & |h_{KK}| & \cdots & |h_{KN}|e^{j(\psi_{KN}-\psi_{KK})} \end{bmatrix} \tag{4}$$

with η denoting the normalization factor to be optimized. The MMSE precoding matrix can then be obtained in a closed form as [32]

$$\mathbf{W}_{\text{MMSE}} = \eta_{\text{MMSE}} \mathbf{H}^{\text{H}} \left(\mathbf{H}\mathbf{H}^{\text{H}} + \frac{K\sigma^2}{p}\mathbf{I} \right)^{-1}, \qquad (8)$$

where

$$\eta_{\text{MMSE}} = \sqrt{\frac{p}{\text{Tr}\left(\mathbf{H}\mathbf{H}^{\text{H}}\left(\mathbf{H}\mathbf{H}^{\text{H}} + (K\sigma^2/p)\mathbf{I}\right)^{-2}\right)}}, \quad (9)$$

denotes the normalization factor ensuring the average transmit power of p. In the case where the measured channel matrix $\hat{\mathbf{H}}$ is used to calculate the MMSE precoding matrix, we obtain

$$
\begin{aligned}
\hat{\mathbf{W}}_{\text{MMSE}}^{\text{D}} &= \hat{\eta}_{\text{MMSE}} \hat{\mathbf{H}}_{\text{D}}^{\text{H}} \left(\hat{\mathbf{H}}_{\text{D}}\hat{\mathbf{H}}_{\text{D}}^{\text{H}} + \frac{K\sigma^2}{p}\mathbf{I} \right)^{-1} \\
&= \hat{\eta}_{\text{MMSE}} \mathbf{H}^{\text{H}}\mathbf{\Psi}_{\text{D}}^{\text{H}} \left(\mathbf{\Psi}_{\text{D}}\mathbf{H}\mathbf{H}^{\text{H}}\mathbf{\Psi}_{\text{D}}^{\text{H}} + \frac{K\sigma^2}{p}\mathbf{\Psi}_{\text{D}}\mathbf{\Psi}_{\text{D}}^{\text{H}} \right)^{-1} \\
&= \hat{\eta}_{\text{MMSE}} \mathbf{H}^{\text{H}}\mathbf{\Psi}_{\text{D}}^{\text{H}}\mathbf{\Psi}_{\text{D}} \left(\mathbf{H}\mathbf{H}^{\text{H}} + \frac{K\sigma^2}{p}\mathbf{I} \right)^{-1}\mathbf{\Psi}_{\text{D}}^{\text{H}} \\
&= \hat{\eta}_{\text{MMSE}} \mathbf{H}^{\text{H}} \left(\mathbf{H}\mathbf{H}^{\text{H}} + \frac{K\sigma^2}{p}\mathbf{I} \right)^{-1}\mathbf{\Psi}_{\text{D}}^{\text{H}}.
\end{aligned}
$$
$$(10)$$

Furthermore, using the symmetry property of $\text{Tr}(\cdot)$ operation, we can write

$$
\begin{aligned}
&\text{Tr}\left(\hat{\mathbf{H}}_{\text{D}}\hat{\mathbf{H}}_{\text{D}}^{\text{H}}\left(\hat{\mathbf{H}}_{\text{D}}\hat{\mathbf{H}}_{\text{D}}^{\text{H}} + (K\sigma^2/p)\mathbf{I}\right)^{-2}\right) \\
&= \text{Tr}\left(\mathbf{\Psi}_{\text{D}}\mathbf{H}\mathbf{H}^{\text{H}}\mathbf{\Psi}_{\text{D}}^{\text{H}}\left(\mathbf{\Psi}_{\text{D}}\mathbf{H}\mathbf{H}^{\text{H}}\mathbf{\Psi}_{\text{D}}^{\text{H}} + (K\sigma^2/p)\mathbf{\Psi}_{\text{D}}\mathbf{\Psi}_{\text{D}}^{\text{H}}\right)^{-2}\right) \\
&= \text{Tr}\left(\mathbf{\Psi}_{\text{D}}\mathbf{H}\mathbf{H}^{\text{H}}\mathbf{\Psi}_{\text{D}}^{\text{H}}\mathbf{\Psi}_{\text{D}}\left(\mathbf{H}\mathbf{H}^{\text{H}} + (K\sigma^2/p)\mathbf{I}\right)^{-2}\mathbf{\Psi}_{\text{D}}^{\text{H}}\right) \\
&= \text{Tr}\left(\mathbf{\Psi}_{\text{D}}^{\text{H}}\mathbf{\Psi}_{\text{D}}\mathbf{H}\mathbf{H}^{\text{H}}\left(\mathbf{H}\mathbf{H}^{\text{H}} + (K\sigma^2/p)\mathbf{I}\right)^{-2}\right) \\
&= \text{Tr}\left(\mathbf{H}\mathbf{H}^{\text{H}}\left(\mathbf{H}\mathbf{H}^{\text{H}} + (K\sigma^2/p)\mathbf{I}\right)^{-2}\right).
\end{aligned}
$$
$$(11)$$

It immediately follows that $\eta_{\text{MMSE}} = \hat{\eta}_{\text{MMSE}}$. As a result, the MMSE precoding matrix under differential phase estimation can be written as

$$\hat{\mathbf{W}}_{\text{MMSE}}^{\text{D}} = \mathbf{W}_{\text{MMSE}}\mathbf{\Psi}_{\text{D}}^{\text{H}}.$$

The UTs' intended symbols precoded with $\hat{\mathbf{W}}_{\text{MMSE}}^{\text{D}}$ are received as

$$
\begin{aligned}
\hat{\mathbf{r}} &= \mathbf{H}\hat{\mathbf{W}}_{\text{MMSE}}^{\text{D}}\mathbf{s} + \mathbf{z} \\
&= \mathbf{\Psi}_{\text{D}}\left(\hat{\eta}_{\text{MMSE}} \mathbf{H}\mathbf{H}^{\text{H}} \left(\mathbf{H}\mathbf{H}^{\text{H}} + \frac{K\sigma^2}{p}\mathbf{I} \right)^{-1}\mathbf{\Psi}_{\text{D}}^{\text{H}}\mathbf{s} + \mathbf{z} \right) \\
&= \hat{\eta}_{\text{MMSE}} \mathbf{\Psi}_{\text{D}}\mathbf{H}\mathbf{H}^{\text{H}} \left(\mathbf{H}\mathbf{H}^{\text{H}} + \frac{K\sigma^2}{p}\mathbf{I} \right)^{-1}\mathbf{\Psi}_{\text{D}}^{\text{H}}\mathbf{s} + \hat{\mathbf{z}}
\end{aligned}
$$
$$(12)$$

To evaluate the effect of differential phase estimation at the UTs on the MMSE precoding performance, we compare the

value of the objective function in (7), denoted by $f_{\text{MMSE}}(\cdot)$, in two cases where $\mathbf{H}$ or $\hat{\mathbf{H}}_{\text{D}}$ is used to calculate the precoding matrix. Given the optimal MMSE precoding matrix and the normalization factor $\hat{\eta}_{\text{MMSE}}$ obtained from the physical channel $\mathbf{H}$, we obtain

$$
\begin{aligned}
&f_{\text{MMSE}}(\mathbf{W}_{\text{MMSE}}, \eta_{\text{MMSE}}) \\
&= \text{E}\left\{ \left\| \mathbf{s} - \eta_{\text{MMSE}}^{-1}(\mathbf{H}\mathbf{W}_{\text{MMSE}}\mathbf{s} + \mathbf{z}) \right\|^2 \right\} \\
&= \text{E}\left\{ \left\| \mathbf{s} - \eta_{\text{MMSE}}^{-1}\mathbf{H}\mathbf{W}_{\text{MMSE}}\mathbf{s} - \eta_{\text{MMSE}}^{-1}\mathbf{z} \right\|^2 \right\} \\
&= \text{E}\left\{ \mathbf{s}^{\text{H}}\mathbf{s} \right\} + \text{E}\left\{ \eta_{\text{MMSE}}^{-2}\mathbf{s}^{\text{H}}\mathbf{W}_{\text{MMSE}}^{\text{H}}\mathbf{H}^{\text{H}}\mathbf{H}\mathbf{W}_{\text{MMSE}}\mathbf{s} \right\} \\
&\quad - 2\text{E}\left\{ \eta_{\text{MMSE}}^{-1}\mathbf{s}^{\text{H}}\mathbf{H}\mathbf{W}_{\text{MMSE}}\mathbf{s} \right\} + \text{E}\left\{ \eta_{\text{MMSE}}^{-2}\mathbf{z}^{\text{H}}\mathbf{z} \right\}, \quad (13)
\end{aligned}
$$

where the last equality holds true under the assumption that $\mathbf{s}$ and $\mathbf{z}$ are uncorrelated. To further simplify (13), we use an equivalent expression for the expectation of quadratic forms provided as follows. Given any square matrix $\mathbf{P}$, it holds true that $\text{E}\{\mathbf{s}^{\text{H}}\mathbf{P}\mathbf{s}\} = \text{Tr}(\mathbf{P}\mathbf{B}) + \mathbf{c}^{\text{H}}\mathbf{P}\mathbf{c}$, where $\mathbf{c} \triangleq \text{E}\{\mathbf{s}\}$ and $\mathbf{B} \triangleq \text{E}\{\mathbf{s}\mathbf{s}^{\text{H}}\} - \text{E}\{\mathbf{s}\}\text{E}\{\mathbf{s}^{\text{H}}\}$. Under the assumption made in Section II that the constellation $\mathbb{X}$ is symmetric w.r.t. the origin, we have $\mathbf{c} = \text{E}\{\mathbf{s}\} = \mathbf{0}$. Moreover, the assumption of $\mathbb{X}$ having unit average power along with the independence of UTs' symbols result in $\text{E}\{\mathbf{s}\mathbf{s}^{\text{H}}\} = \mathbf{I}$, yielding $\mathbf{B} = \mathbf{I}$. As a consequence, $\text{E}\{\mathbf{s}^{\text{H}}\mathbf{P}\mathbf{s}\} = \text{Tr}(\mathbf{P})$ holds true. Thereby, we can write (13) as

$$
\begin{aligned}
&f_{\text{MMSE}}(\mathbf{W}_{\text{MMSE}}, \eta_{\text{MMSE}}) \\
&= \text{E}\left\{ \mathbf{s}^{\text{H}}\mathbf{s} \right\} + \eta_{\text{MMSE}}^{-2}\text{Tr}\left(\mathbf{W}_{\text{MMSE}}^{\text{H}}\mathbf{H}^{\text{H}}\mathbf{H}\mathbf{W}_{\text{MMSE}} \right) \\
&\quad - 2\eta_{\text{MMSE}}^{-1}\text{Tr}\left(\mathbf{H}\mathbf{W}_{\text{MMSE}} \right) + \text{E}\left\{ \eta_{\text{MMSE}}^{-2}\mathbf{z}^{\text{H}}\mathbf{z} \right\}. \quad (14)
\end{aligned}
$$

On the other hand, with $\hat{\mathbf{W}}_{\text{MMSE}}$, the objective function of the MMSE design evaluates as

$$
\begin{aligned}
&f_{\text{MMSE}}(\hat{\mathbf{W}}_{\text{MMSE}}^{\text{D}}, \hat{\eta}_{\text{MMSE}}) \\
&= \text{E}\left\{ \left\| \mathbf{s} - \hat{\eta}_{\text{MMSE}}^{-1}\mathbf{\Psi}_{\text{D}}(\mathbf{H}\hat{\mathbf{W}}_{\text{MMSE}}^{\text{D}}\mathbf{s} + \mathbf{z}) \right\|^2 \right\} \\
&= \text{E}\left\{ \left\| \mathbf{s} - \eta_{\text{MMSE}}^{-1}\mathbf{\Psi}_{\text{D}}\mathbf{H}\mathbf{W}_{\text{MMSE}}\mathbf{\Psi}_{\text{D}}^{\text{H}}\mathbf{s} - \eta_{\text{MMSE}}^{-1}\mathbf{\Psi}_{\text{D}}\mathbf{z} \right\|^2 \right\} \\
&= \text{E}\left\{ \mathbf{s}^{\text{H}}\mathbf{s} \right\} + \text{E}\left\{ \eta_{\text{MMSE}}^{-2}\mathbf{s}^{\text{H}}\mathbf{\Psi}_{\text{D}}\mathbf{W}_{\text{MMSE}}^{\text{H}}\mathbf{H}^{\text{H}}\mathbf{H}\mathbf{W}_{\text{MMSE}}\mathbf{\Psi}_{\text{D}}^{\text{H}}\mathbf{s} \right\} \\
&\quad - 2\text{E}\left\{ \eta_{\text{MMSE}}^{-1}\mathbf{s}^{\text{H}}\mathbf{\Psi}_{\text{D}}\mathbf{H}\mathbf{W}_{\text{MMSE}}\mathbf{\Psi}_{\text{D}}^{\text{H}}\mathbf{s} \right\} + \text{E}\left\{ \eta_{\text{MMSE}}^{-2}\mathbf{z}^{\text{H}}\mathbf{z} \right\},
\end{aligned}
$$
$$(15)$$

Similarly, using $\mathrm{E}\{\mathbf{s}^{\mathrm{H}}\mathbf{P}\mathbf{s}\} = \mathrm{Tr}(\mathbf{P})$, we can simplify (15) as

$$f_{\mathrm{MMSE}}(\hat{\mathbf{W}}_{\mathrm{MMSE}}^{\mathrm{D}}, \hat{\eta}_{\mathrm{MMSE}})$$

$$= \mathrm{E}\left\{\mathbf{s}^{\mathrm{H}}\mathbf{s}\right\} + \eta_{\mathrm{MMSE}}^{-2}\mathrm{Tr}\left(\boldsymbol{\Psi}_{\mathrm{D}}\mathbf{W}_{\mathrm{MMSE}}^{\mathrm{H}}\mathbf{H}^{\mathrm{H}}\mathbf{H}\mathbf{W}_{\mathrm{MMSE}}\boldsymbol{\Psi}_{\mathrm{D}}^{\mathrm{H}}\right)$$

$$- 2\eta_{\mathrm{MMSE}}^{-1}\mathrm{Tr}\left(\boldsymbol{\Psi}_{\mathrm{D}}\mathbf{H}\mathbf{W}_{\mathrm{MMSE}}\boldsymbol{\Psi}_{\mathrm{D}}^{\mathrm{H}}\right) + \mathrm{E}\left\{\eta_{\mathrm{MMSE}}^{-2}\mathbf{z}^{\mathrm{H}}\mathbf{z}\right\}$$

$$= \mathrm{E}\left\{\mathbf{s}^{\mathrm{H}}\mathbf{s}\right\} + \eta_{\mathrm{MMSE}}^{-2}\mathrm{Tr}\left(\boldsymbol{\Psi}_{\mathrm{D}}^{\mathrm{H}}\boldsymbol{\Psi}_{\mathrm{D}}\mathbf{W}_{\mathrm{MMSE}}^{\mathrm{H}}\mathbf{H}^{\mathrm{H}}\mathbf{H}\mathbf{W}_{\mathrm{MMSE}}\right)$$

$$- 2\eta_{\mathrm{MMSE}}^{-1}\mathrm{Tr}\left(\boldsymbol{\Psi}_{\mathrm{D}}^{\mathrm{H}}\boldsymbol{\Psi}_{\mathrm{D}}\mathbf{H}\mathbf{W}_{\mathrm{MMSE}}\right) + \mathrm{E}\left\{\eta_{\mathrm{MMSE}}^{-2}\mathbf{z}^{\mathrm{H}}\mathbf{z}\right\}$$

$$= \mathrm{E}\left\{\mathbf{s}^{\mathrm{H}}\mathbf{s}\right\} + \eta_{\mathrm{MMSE}}^{-2}\mathrm{Tr}\left(\mathbf{W}_{\mathrm{MMSE}}^{\mathrm{H}}\mathbf{H}^{\mathrm{H}}\mathbf{H}\mathbf{W}_{\mathrm{MMSE}}\right)$$

$$- 2\eta_{\mathrm{MMSE}}^{-1}\mathrm{Tr}\left(\mathbf{H}\mathbf{W}_{\mathrm{MMSE}}\right) + \mathrm{E}\left\{\eta_{\mathrm{MMSE}}^{-2}\mathbf{z}^{\mathrm{H}}\mathbf{z}\right\}, \qquad (16)$$

From (14) and (16), it is evident that

$$f_{\mathrm{MMSE}}(\mathbf{W}_{\mathrm{MMSE}}, \eta_{\mathrm{MMSE}}) = f_{\mathrm{MMSE}}(\hat{\mathbf{W}}_{\mathrm{MMSE}}^{\mathrm{D}}, \hat{\eta}_{\mathrm{MMSE}}).$$

As a result, both $\mathbf{W}_{\mathrm{MMSE}}$ and $\hat{\mathbf{W}}_{\mathrm{MMSE}}^{\mathrm{D}}$ lead to the same value for the objective function of the MMSE design problem. Recall, further, that $\eta_{\mathrm{MMSE}} = \hat{\eta}_{\mathrm{MMSE}}$, i.e., the average transmitted power is the same with either $\mathbf{W}_{\mathrm{MMSE}}$ or $\hat{\mathbf{W}}_{\mathrm{MMSE}}^{\mathrm{D}}$. Therefore, we conclude that the MMSE precoding's performance is preserved under differential phase estimation at the UTs' receivers.

The equivalent demonstration for ZF can be easily obtained by making zero the term $\frac{K\sigma^2}{p}\mathbf{I}$ in (8) and (9) since the Precoding matrix for ZF is calculated according to

$$\mathbf{W}_{\mathrm{ZF}} = \eta_{\mathrm{ZF}}\mathbf{H}^{\mathrm{H}}\left(\mathbf{H}\mathbf{H}^{\mathrm{H}}\right)^{-1}, \qquad (17)$$

where

$$\eta_{\mathrm{ZF}} = \sqrt{\frac{p}{\mathrm{Tr}\left(\left(\mathbf{H}\mathbf{H}^{\mathrm{H}}\right)^{-1}\right)}} \qquad (18)$$

A similar analysis considering the noise introduced by the frequency down-conversion at the transponder leads to

$$\hat{\mathbf{W}}_{\mathrm{MMSE}}^{\mathrm{U}} = \boldsymbol{\Phi}_{\mathrm{U}}^{\mathrm{H}}(t)\mathbf{W}_{\mathrm{MMSE}}. \qquad (19)$$

However, in this case the received signal at the UTs is

$$\hat{\mathbf{r}} = \mathbf{H}_{\mathrm{U}}\hat{\mathbf{W}}_{\mathrm{MMSE}}^{\mathrm{U}}\mathbf{s} + \mathbf{z}$$

$$= \mathbf{H}\boldsymbol{\Phi}_{\mathrm{U}}(t_0 + \tau)\boldsymbol{\Phi}_{\mathrm{U}}^{\mathrm{H}}(t_0)\mathbf{W}_{\mathrm{MMSE}}\mathbf{s} + \mathbf{z}$$

$$= \eta_{\mathrm{MMSE}}\mathbf{s} + \mathbf{z}. \qquad (20)$$

Equation (20) suggests that the precoding loop compensates for the phase errors introduced in the transponder, which is true, but it only holds under certain conditions. The multiplication $\boldsymbol{\Phi}_{\mathrm{U}}(t_0 + \tau)\boldsymbol{\Phi}_{\mathrm{U}}^{\mathrm{H}}(t_0) = \mathbf{I}$ assumes that the phase noise remains constant between the estimation of the CSI $\boldsymbol{\Phi}_{\mathrm{U}}^{\mathrm{H}}(t_0)$ at time t_0 and the use of the precoding matrix $\boldsymbol{\Phi}_{\mathrm{U}}(t_0 + \tau)$ after a delay τ. This assumption can be valid for specific conditions where the distance between transmitter and receiver is small, such as some terrestrial networks, and for excellent frequency references, which is not the general case in GEO satellite systems. As a result, we can conclude that the phase noise introduced by the transponder affects the performance of linear precoding systems. This demonstration can be easily extended to other linear precoding methods such as ZF.

B. SYMBOL-LEVEL PRECODING

A SLP technique directly calculates the precoded transmit signal (hence, no precoding matrix) on a symbol-by-symbol basis by exploiting the UTs' instantaneous data symbols. Accordingly, the transmit signal is designed so that each UT's (noise-free) received signal is located within the so-called constructive interference region (CIR) corresponding to its intended symbol. The CIRs are typically defined to improve the symbol detection accuracy at the receiver side; hence, they depend on the modulation scheme in use. These regions have been defined in several different ways in the literature; see, e.g., [33], [34], [35]. In this work, we focus on a specific family of CIRs, namely, distance-preserving CIRs [35], which are presented in a generic form that applies to any given modulation scheme. This general family of CIRs will be described in detail in the next section. For the moment, let us focus on the resulting SLP design problem. In what follows, we use the equivalent real-valued notations introduced in Section II.

Let $\mathbf{u}$ denote the complex-valued $N \times 1$ precoded transmit vector to be directly obtained as a result of solving the SLP optimization problem. We further denote the equivalent real-valued representation of $\mathbf{u}$ by $\bar{\mathbf{u}} \triangleq [\mathrm{Re}(\mathbf{u}), \mathrm{Im}(\mathbf{u})]^{\mathrm{T}}$. Assume, also, that a set of SNIR requirements $\{\gamma_1, \dots, \gamma_K\}$ are provided to be met for the UTs. Then, given the physical channel $\bar{\mathbf{H}}$, the power minimization SLP problem under distance-preserving CIR constraints can be expressed as

$$\min_{\bar{\mathbf{u}}, \mathbf{d}} \quad \|\bar{\mathbf{u}}\|^2 \quad \text{s.t.} \quad \mathbf{A}(\bar{\mathbf{H}}\bar{\mathbf{u}} - \boldsymbol{\Sigma}\boldsymbol{\Gamma}\bar{\mathbf{s}}) = \mathbf{d}, \; \mathbf{d} \succeq \mathbf{0}, \qquad (21)$$

where the following definitions are used: $\bar{\mathbf{H}} \triangleq [\bar{\mathbf{H}}_1^{\mathrm{T}}, \dots, \bar{\mathbf{H}}_K^{\mathrm{T}}]^{\mathrm{T}}$; $\mathbf{A} \triangleq \mathrm{blkdiag}(\mathbf{A}_1, \dots, \mathbf{A}_K)$ with $\mathbf{A}_k = [\mathbf{a}_{k,1}, \mathbf{a}_{k,2}]^{\mathrm{T}}$ and $\mathbf{a}_{k,1}$ and $\mathbf{a}_{k,2}$ denoting the normal vectors of the maximum-likelihood (ML) decision boundaries (Voronoi regions) of $\mathbf{s}_k$; $\boldsymbol{\Sigma} \triangleq \mathrm{diag}(\sigma_1, \dots, \sigma_K) \otimes \mathbf{I}_2$; $\boldsymbol{\Gamma} \triangleq \mathrm{diag}(\sqrt{\gamma_1}, \dots, \sqrt{\gamma_K}) \otimes \mathbf{I}_2$; $\mathbf{s} \triangleq [\mathbf{s}_1, \dots, \mathbf{s}_K]^{\mathrm{T}}$; and $\mathbf{d} \triangleq [\mathbf{d}_1^{\mathrm{T}}, \dots, \mathbf{d}_K^{\mathrm{T}}]^{\mathrm{T}}$ is a $2K \times 1$ vector of distances between the received symbols, without noise, and the DPCIR edges. The elements $\mathbf{d}_k$ are 2×1 vectors defined as $\mathbf{d}_k \triangleq [d_{k,1}, d_{k,2}]^{\mathrm{T}}$ for all $k = 1, \dots, K$. Equivalently, the optimal symbol-level precoded transmit vector can be obtained by the following lemma [36].

Lemma 1: Given the physical channel $\bar{\mathbf{H}}$, the minimum-power precoded signal vector satisfying the distance-preserving constructive interference (CI) constraint of (21) is given by

$$\bar{\mathbf{u}} = \bar{\mathbf{H}}^{\dagger}\left(\boldsymbol{\Sigma}\boldsymbol{\Gamma}\bar{\mathbf{s}} + \mathbf{A}^{-1}\mathbf{d}\right), \qquad (22)$$

where $\mathbf{d}$ is the optimal solution to the following non-negative least squares (NNLS) problem

$$\min_{\mathbf{d} \geq 0} \quad \|\bar{\mathbf{H}}^{\dagger}\boldsymbol{\Sigma}\boldsymbol{\Gamma}\bar{\mathbf{s}} + \mathbf{H}^{\dagger}\mathbf{A}^{-1}\mathbf{d}\|^2. \qquad (23)$$

Having the optimal precoded vector provided by Lemma1, we can obtain the received signal vector at the UTs' as

$$\mathbf{r} = \bar{\mathbf{H}}\bar{\mathbf{u}} + \bar{\mathbf{z}}$$
$$= \bar{\mathbf{H}}\bar{\mathbf{H}}^{\dagger}\left(\boldsymbol{\Sigma}\boldsymbol{\Gamma}\bar{\mathbf{s}} + \mathbf{A}^{-1}\mathbf{d}\right) + \bar{\mathbf{z}}$$
$$= \boldsymbol{\Sigma}\boldsymbol{\Gamma}\bar{\mathbf{s}} + \mathbf{A}^{-1}\mathbf{d} + \bar{\mathbf{z}}. \qquad (24)$$

Now, assume that instead of the physical channel matrix $\mathbf{H}$, the measured channel $\hat{\mathbf{H}}_{\mathrm{D}}$ is given to calculate $\bar{\mathbf{u}}$. Let us denote by $\hat{\bar{\mathbf{H}}}_{\mathrm{D}}$ the equivalent real-valued representation of $\hat{\mathbf{H}}_{\mathrm{D}}$. Then, the relation between $\bar{\mathbf{H}}$ and $\hat{\bar{\mathbf{H}}}_{\mathrm{D}}$ in the real domain is given as

$$\hat{\bar{\mathbf{H}}}_{\mathrm{D}} = \bar{\boldsymbol{\Psi}}_{\mathrm{D}}\bar{\mathbf{H}}, \qquad (25)$$

where $\bar{\boldsymbol{\Psi}}_{\mathrm{D}} \triangleq \mathrm{blkdiag}(\boldsymbol{\Psi}_{\mathrm{D}_1}, \ldots, \boldsymbol{\Psi}_{\mathrm{D}_K})$ with

$$\boldsymbol{\Psi}_{\mathrm{D}_k} = \begin{bmatrix} \mathrm{Re}(e^{-\mathrm{j}\psi_{kk}}) & -\mathrm{Im}(e^{-\mathrm{j}\psi_{kk}}) \\ \mathrm{Im}(e^{-\mathrm{j}\psi_{kk}}) & \mathrm{Re}(e^{-\mathrm{j}\psi_{kk}}), \end{bmatrix}$$

for any $k \in \{1, 2, \ldots, K\}$. According to this definition, we can simplify $\bar{\boldsymbol{\Psi}}_{\mathrm{D}}$ as shown in (26) at the bottom of this page where each block of $\bar{\boldsymbol{\Psi}}_{\mathrm{D}}$ is a two-dimensional rotation matrix. In this case, we obtain

$$\hat{\bar{\mathbf{u}}} = \hat{\bar{\mathbf{H}}}^{\dagger}\left(\boldsymbol{\Sigma}\boldsymbol{\Gamma}\bar{\mathbf{s}} + \mathbf{A}^{-1}\hat{\mathbf{d}}\right)$$
$$= (\bar{\boldsymbol{\Psi}}_{\mathrm{D}}\bar{\mathbf{H}})^{\dagger}\left(\boldsymbol{\Sigma}\boldsymbol{\Gamma}\bar{\mathbf{s}} + \mathbf{A}^{-1}\hat{\mathbf{d}}\right)$$
$$= \bar{\mathbf{H}}^{\dagger}\bar{\boldsymbol{\Psi}}_{\mathrm{D}}^{-1}\left(\boldsymbol{\Sigma}\boldsymbol{\Gamma}\bar{\mathbf{s}} + \mathbf{A}^{-1}\hat{\mathbf{d}}\right), \qquad (27)$$

Accordingly, the vector $\hat{\mathbf{d}}$ is obtained as the solution to the following NNLS problem:

$$\min_{\hat{\mathbf{d}} \geq \mathbf{0}} \quad \|\bar{\mathbf{H}}^{\dagger}\boldsymbol{\Sigma}\boldsymbol{\Gamma}\bar{\boldsymbol{\Psi}}_{\mathrm{D}}^{-1}\bar{\mathbf{s}} + \bar{\mathbf{H}}^{\dagger}\bar{\boldsymbol{\Psi}}_{\mathrm{D}}^{-1}\mathbf{A}^{-1}\hat{\mathbf{d}}\|^2. \qquad (28)$$

where in deriving (28), we have used the property that diagonal matrices are commutative, i.e., $\bar{\boldsymbol{\Psi}}_{\mathrm{D}}^{\dagger}\boldsymbol{\Sigma}\boldsymbol{\Gamma} = \boldsymbol{\Sigma}\boldsymbol{\Gamma}\bar{\boldsymbol{\Psi}}_{\mathrm{D}}^{\dagger}$. Having the precoded vector (27), the UTs' received signal in the real domain can be expressed as

$$\hat{\mathbf{r}} = \bar{\boldsymbol{\Psi}}_{\mathrm{D}}\left(\bar{\mathbf{H}}\hat{\bar{\mathbf{u}}} + \bar{\mathbf{z}}\right)$$
$$= \bar{\boldsymbol{\Psi}}_{\mathrm{D}}\left(\bar{\mathbf{H}}\bar{\mathbf{H}}^{\dagger}\bar{\boldsymbol{\Psi}}_{\mathrm{D}}^{-1}\left(\boldsymbol{\Sigma}\boldsymbol{\Gamma}\bar{\mathbf{s}} + \mathbf{A}^{-1}\hat{\mathbf{d}}\right) + \bar{\mathbf{z}}\right)$$
$$= \boldsymbol{\Sigma}\boldsymbol{\Gamma}\bar{\mathbf{s}} + \mathbf{A}^{-1}\hat{\mathbf{d}} + \bar{\boldsymbol{\Psi}}_{\mathrm{D}}\bar{\mathbf{z}}$$
$$= \boldsymbol{\Sigma}\boldsymbol{\Gamma}\bar{\mathbf{s}} + \mathbf{A}^{-1}\hat{\mathbf{d}} + \hat{\bar{\mathbf{z}}}, \qquad (29)$$

where $\hat{\bar{\mathbf{z}}} \triangleq \bar{\boldsymbol{\Psi}}_{\mathrm{D}}\bar{\mathbf{z}}$ is a CSCG vector with zero mean and variance σ^2. Comparing (24) with (29), we can see that the

received signal vector $\hat{\mathbf{r}}$ with phase-normalized channel resembles in form to $\mathbf{r}$ obtained with the physical channel. However, they differ from each other in the vector-valued variables $\mathbf{d}$ and $\hat{\mathbf{d}}$, which are not equal in general since they are solutions to two different optimization problems.

In the NNLS problem (28), $\mathbf{A}^{-1}$ and $\bar{\mathbf{s}}$ are rotated as

$$\bar{\boldsymbol{\Psi}}_{\mathrm{D}}^{-1}\mathbf{A}^{-1} = \begin{bmatrix} \boldsymbol{\Psi}_{\mathrm{D}_1} & \cdots & 0 \\ \vdots & \ddots & \vdots \\ 0 & \cdots & \boldsymbol{\Psi}_{\mathrm{D}_K} \end{bmatrix}^{-1} \times \begin{bmatrix} \mathbf{A}_1 & \cdots & 0 \\ \vdots & \ddots & \vdots \\ 0 & \cdots & \mathbf{A}_K \end{bmatrix}^{-1}$$

$$= \begin{bmatrix} \boldsymbol{\Psi}_{\mathrm{D}_1}^{-1}\mathbf{A}_1^{-1} & \cdots & 0 \\ \vdots & \ddots & \vdots \\ 0 & \cdots & \boldsymbol{\Psi}_{\mathrm{D}_K}^{-1}\mathbf{A}_K^{-1} \end{bmatrix}, \qquad (30)$$

and

$$\bar{\boldsymbol{\Psi}}_{\mathrm{D}}^{-1}\bar{\mathbf{s}} = \begin{bmatrix} \boldsymbol{\Psi}_{\mathrm{D}_1} & \cdots & 0 \\ \vdots & \ddots & \vdots \\ 0 & \cdots & \boldsymbol{\Psi}_{\mathrm{D}_K} \end{bmatrix}^{-1} \times \begin{bmatrix} \mathbf{s}_1 \\ \vdots \\ \mathbf{s}_K \end{bmatrix} = \begin{bmatrix} \boldsymbol{\Psi}_{\mathrm{D}_1}^{-1}\mathbf{s}_1 \\ \vdots \\ \boldsymbol{\Psi}_{\mathrm{D}_K}^{-1}\mathbf{s}_K \end{bmatrix}. \qquad (31)$$

from which it follows that each symbol $\mathbf{s}_k$ and its corresponding sub-matrix $\mathbf{A}_k$ are rotated by ψ_{kk}. Note that the distance-preserving CIR of $\mathbf{s}_k$ can be identified by $\mathbf{s}_k$ and its matrix of normal vectors $\mathbf{A}_k$. Keeping in mind that the same angular value rotates both $\mathbf{s}_k$ and $\mathbf{A}_k$, we can interpret this rotation as follows. With phase rotated channel $\hat{\bar{\mathbf{H}}}_{\mathrm{D}}$, the constellation sets of UTs, at any given symbol period, are rotated versions of their original constellations, where the rotation angles correspond to those in the rotation matrix $\bar{\boldsymbol{\Psi}}_{\mathrm{D}}$. It is important to note that the symbol constellation of each UT undergoes a rotation by an angular value that corresponds to the reference phase value of its own channel vector. Therefore, the UTs' constellations are not equally rotated in general. In Fig. 4, we illustrate how the intended symbols and their corresponding distance-preserving CIRs of two different UTs may be rotated. It can be seen that the relative positioning of the constellation symbols is preserved under this rotation. Further, the shape of distance-preserving CIRs (including the angle between their two edges) remains unchanged. As a result, the relative geometry of the constellation is preserved under differential phase estimation.

Let us denote $\bar{\mathbf{s}}_{\mathrm{r}} \triangleq \bar{\boldsymbol{\Psi}}_{\mathrm{D}}^{-1}\bar{\mathbf{s}}$ and $\mathbf{A}_{\mathrm{r}}^{-1} \triangleq \bar{\boldsymbol{\Psi}}_{\mathrm{D}}^{-1}\mathbf{A}^{-1}$. Then, the following lemma encapsulates the solution of the SLP problem in the case with differential phase estimation.

$$\bar{\boldsymbol{\Psi}}_{\mathrm{D}} = \begin{bmatrix} \cos(\psi_{11}) & \sin(\psi_{11}) & \cdots & 0 & 0 \\ -\sin(\psi_{11}) & \cos(\psi_{11}) & \cdots & 0 & 0 \\ \vdots & \vdots & \ddots & \vdots & \vdots \\ 0 & 0 & \cdots & \cos(\psi_{KK}) & \sin(\psi_{KK}) \\ 0 & 0 & \cdots & -\sin(\psi_{KK}) & \cos(\psi_{KK}) \end{bmatrix} \qquad (26)$$
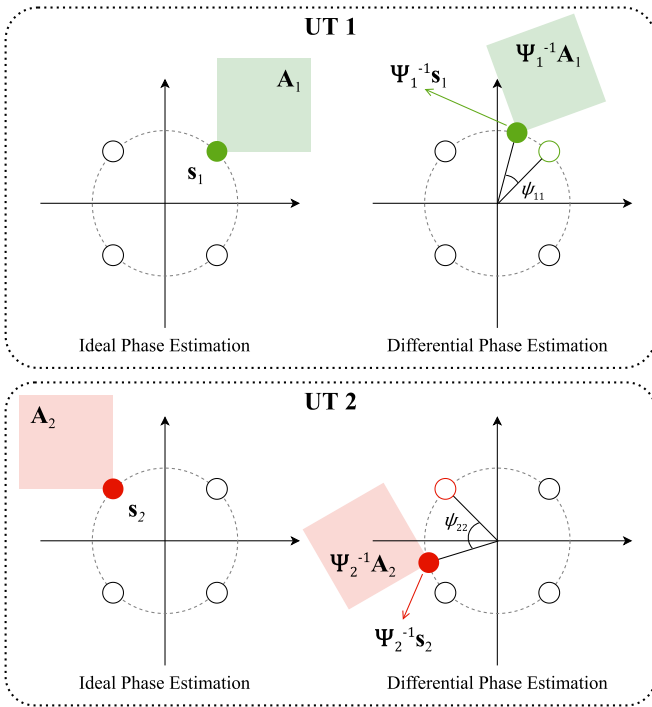
FIGURE 4. An illustrative example of original and rotated QPSK symbols and their corresponding distance-preserving CIRs.

Lemma 2: Given the phase-normalized channel $\hat{\bar{\mathbf{H}}}_D$, with rotation matrix $\bar{\mathbf{\Psi}}_D$, the minimum-power solution of the SLP design under distance-preserving CI constraints is given by

$$\hat{\mathbf{u}} = \bar{\mathbf{H}}^{\dagger} \left(\mathbf{\Sigma}\mathbf{\Gamma}\bar{\mathbf{s}}_r + \mathbf{A}_r^{-1}\hat{\mathbf{d}} \right), \tag{32}$$

where $\hat{\mathbf{d}}$ is the optimal solution to the following NNLS problem

$$\min_{\hat{\mathbf{d}} \succeq \mathbf{0}} \quad \| \bar{\mathbf{H}}^{\dagger} \mathbf{\Sigma}\mathbf{\Gamma}\bar{\mathbf{s}}_r + \mathbf{H}^{\dagger}\mathbf{A}_r^{-1}\hat{\mathbf{d}} \|^2, \tag{33}$$

with $\bar{\mathbf{s}}_r$ and $\mathbf{A}_r^{-1}$ representing rotated constellations w.r.t. the original ones.

The difference between the SLP design with the physical channel $\bar{\mathbf{H}}$, and the one with the phase-normalized channel $\hat{\bar{\mathbf{H}}}_D$ originates from the vector-valued design variables $\mathbf{d}$ and $\hat{\mathbf{d}}$ as the solutions to the NNLS problems (23) and (33), respectively. In fact, given the channel matrix and the UTs' symbols, this is the design variable that controls the performance of the SLP. Now, the question is how the performance differs in these two cases. In other words, how the differential phase estimation process affects the SLP's performance. Based on the above discussion, we should analyze the NNLS problem associated with the SLP design and its dependency on different parameters to answer this question. The following theorem states the result of such an analysis, where its proof is provided in the next section.

Theorem 3: The average performance of an SNIR-constrained power minimization SLP design with distance-preserving CIR constraints is preserved under differential phase estimation.

The proof of Theorem 3 is not straightforward, but it requires a closer look into the structure of the SLP's NNLS formulation, as we will see in Section V.

V. ANALYSIS OF THE NNLS-BASED SLP DESIGN

This section analyzes the solution to the SLP problem with distance-preserving CI constraints to reveal its dependency on the constellation-dependent design parameters. More specifically, the main result of this section is the proof of Theorem 3. To this end, we derive an explicit function that can assess the SLP's performance as a function of the constellation parameters. The results can be applied in the SLP design process. Expecificly, for the cases where the phase-normalized channel $\hat{\bar{\mathbf{H}}}_D$ is modelled as rotated UTs' constellations.

We mentioned earlier in Section IV that differential phase estimation at the UTs and its subsequent effects on the SLP design at the transmitter can be modelled as a rotation applied to the symbol constellation of each UT. This rotation preserves the relative geometry of the constellation; however, the symbols' exact positioning and corresponding CIRs will be affected. Therefore, it becomes interesting to know whether the average performance of SLP depends on the relative or the exact geometry of the constellation, or even on both.

Let us start our analysis by reviewing the characteristics and definitions of distance-preserving CIRs. Recall that the UTs' intended symbols are taken from the constellation set $\mathbb{X}$, i.e., $s_k = x_i$ for some $x_i \in \mathbb{X}$. In the sequel, with a slight deviation in notation, we use the subscript i for the matrix $\mathbf{A}$ and the vector $\mathbf{d}$ that corresponds to the ith constellation symbol.

As defined in [36], any two points belonging to two distinct distance-preserving CIRs are distanced by at least the distance between the corresponding constellation symbols. Therefore, given a constellation point $\mathbf{x}_i$, any $\mathbf{x} \in \mathbb{R}^2$ belonging to the distance-preserving CIR of $\mathbf{x}_i$ satisfies

$$\mathbf{A}_i \left(\mathbf{x} - \mathbf{x}_i \right) = \mathbf{d}_i, \quad \text{where} \begin{cases} \mathbf{d}_i \succeq \mathbf{0}, & \mathbf{x}_i \in \mathbf{bd}(\mathbb{X}), \\ \mathbf{d}_i = \mathbf{0}, & \mathbf{x}_i \in \mathbf{int}(\mathbb{X}). \end{cases} \tag{34}$$

where $\mathbf{A}_i = [\mathbf{a}_{i,1}, \mathbf{a}_{i,2}]^T$ contains the normal vectors of the maximum-likelihood (ML) decision boundaries (Voronoi regions) of $\mathbf{x}_i$. The two normal vectors $\mathbf{a}_{i,1}$ and $\mathbf{a}_{i,2}$ can simply be obtained using the following criteria:

- If $\mathbf{x}_i \in \mathbf{bd}(\mathbb{X})$, we obtain $\mathbf{a}_{i,1}$ and $\mathbf{a}_{i,2}$ by subtracting symbol $\mathbf{x}_i$ from its two neighboring constellation points on $\mathbf{bd}(\mathbb{X})$, namely, $\mathbf{x}_{i,1}$ and $\mathbf{x}_{i,2}$. In this case, we have

$$\mathbf{A}_i = \begin{bmatrix} \mathbf{a}_{i,1}^T \\ \mathbf{a}_{i,2}^T \end{bmatrix} = \begin{bmatrix} (\mathbf{x}_i - \mathbf{x}_{i,1})^T \\ (\mathbf{x}_i - \mathbf{x}_{i,2})^T \end{bmatrix} \in \mathbb{R}^{2 \times 2}.$$

- If $\mathbf{x}_i \in \mathbf{int}(\mathbb{X})$, we set $\mathbf{a}_{i,1} = \mathbf{0}$ and $\mathbf{a}_{i,2} = \mathbf{0}$, and therefore, we have $\mathbf{A}_i = \mathbf{0} \in \mathbb{R}^{2 \times 2}$.

Without loss of generality, let us further assume that, for any $\mathbf{x}_i \in \mathbf{bd}(\mathbb{X})$, the normal vectors $\mathbf{a}_{i,1}$ and $\mathbf{a}_{i,2}$ are normalized such that $\|\mathbf{a}_{i,1}\| = \|\mathbf{a}_{i,2}\| = 1$. It is worth noting that such an assumption does not affect the inequality (34). Accordingly, we have

$$\mathbf{A}_i \mathbf{A}_i^{\mathrm{T}} = \begin{bmatrix} \mathbf{a}_{i,1}^{\mathrm{T}} \mathbf{a}_{i,1} & \mathbf{a}_{i,1}^{\mathrm{T}} \mathbf{a}_{i,2} \\ \mathbf{a}_{i,2}^{\mathrm{T}} \mathbf{a}_{i,1} & \mathbf{a}_{i,2}^{\mathrm{T}} \mathbf{a}_{i,2}^{\mathrm{T}} \end{bmatrix} = \begin{bmatrix} 1 & \cos\phi_i \\ \cos\phi_i & 1 \end{bmatrix}, \quad (35)$$

where $\phi_i \triangleq \angle(\mathbf{a}_{i,1}, \mathbf{a}_{i,2})$ denotes the angle between the normal vectors $\mathbf{a}_{i,1}$ and $\mathbf{a}_{i,2}$. From (35), it further follows that

$$(\mathbf{A}_i \mathbf{A}_i^{\mathrm{T}})^{-1} = \frac{1}{\sin^2\phi_i} \begin{bmatrix} 1 & -\cos\phi_i \\ -\cos\phi_i & 1 \end{bmatrix}. \quad (36)$$

Next, let us focus on the NNLS problem in (23), which is the key step in the derivation of the optimal SLP solution. Denoting $\mathbf{Q} \triangleq -\bar{\mathbf{H}}^\dagger \mathbf{A}^{-1}$ and $\mathbf{y} \triangleq \bar{\mathbf{H}}^\dagger \mathbf{\Sigma} \mathbf{\Gamma} \bar{\mathbf{s}}$, we can rewrite the NNLS optimization (23) in the standard form as

$$\min_{\mathbf{d} \succeq \mathbf{0}} \quad \|\mathbf{y} - \mathbf{Q}\mathbf{d}\|^2. \quad (37)$$

It can be easily verified that the optimum of (37) can be equally achieved by the following dimensionality-reduced problem:

$$\min_{\mathbf{d}_r \succeq \mathbf{0}} \quad \|\mathbf{y} - \mathbf{Q}_r \mathbf{d}_r\|^2, \quad (38)$$

where $[\bar{\mathbf{H}}^\dagger]_r$ denotes the matrix obtained by removing those columns of $\bar{\mathbf{H}}^\dagger$ that correspond to the UTs with a symbol in $\mathbf{int}(\mathbb{X})$, and similarly, $[\mathbf{A}^{-1}]_{r,r}$ denotes the matrix obtained by removing those columns and rows of $\mathbf{A}^{-1}$ that correspond to the UTs with a symbol in $\mathbf{int}(\mathbb{X})$. Therefore, $\mathbf{Q}_r \triangleq -[\bar{\mathbf{H}}^\dagger]_r [\mathbf{A}^{-1}]_{r,r}$ is a $2N \times 2L$ matrix, with L denoting the number of UTs with a symbol in $\mathbf{bd}(\mathbb{X})$. As a result, the equivalent NNLS design in (38) has a dimension of $2L$, where $L \leq K$. Any minimizer $\mathbf{d}^*$ of the original design can simply be obtained by appropriately padding $\mathbf{d}_r^*$ with $2K - 2L$ zeros.

A. SPARSITY ANALYSIS OF THE NNLS DESIGN

To analyze the sparsity of the (unique) solution to the NNLS problem in (37), we start from a quantitative measure called *separation quantity* [37], which is defined as

$$\tau^2 \triangleq \min_{\mathbf{p} \in \mathcal{S}^{2L-1}} \frac{1}{2L} \mathbf{p}^{\mathrm{T}} \mathbf{Q}_r^{\mathrm{T}} \mathbf{Q}_r \mathbf{p}, \quad (39)$$

where $\mathcal{S}^n = \{\mathbf{p} \in \mathbb{R}^{n+1} : \mathbf{1}^{\mathrm{T}} \mathbf{p} = 1, \ \mathbf{p} \succeq \mathbf{0}\}$ represents an n-simplex (i.e., an n-dimensional simplex with $n-1$ degrees of freedom), and $1/(2L)$ is a normalization factor with respect to the problem size. From a geometric point of view, τ equals the orthogonal distance of the convex hull of the columns of $\mathbf{Q}_r$ to the origin. This quantity can be used to determine whether the non-negativity constraints are effective, otherwise, the optimization in (38) is nothing more than an ordinary least squares problem. Moreover, none of the non-negativity constraints introduced by the element-wise inequality $\mathbf{d}_r \succeq \mathbf{0}$ is

active if $\tau > 0$ does not hold true. This elementary condition is always satisfied for the NNLS design in (38). Due to the facts that $\mathbf{Q}_r$ is a full column rank matrix and that $\mathbf{Q}_r^{\mathrm{T}} \mathbf{Q}_r$ is symmetric, we have $\mathbf{Q}_r^{\mathrm{T}} \mathbf{Q}_r > 0$, i.e., $\mathbf{Q}_r^{\mathrm{T}} \mathbf{Q}_r$ is positive definite. Hence $\mathbf{p}^{\mathrm{T}} \mathbf{Q}_r^{\mathrm{T}} \mathbf{Q}_r \mathbf{p} > 0$ for all $\mathbf{p} \neq \mathbf{0}$. Note that the positive definiteness is sufficient here since the constraint $\mathbf{p} \in \mathcal{S}^{2L-1}$ prevents the case $\mathbf{p} = \mathbf{0}$ in our problem. In light of the separation quantity (39), a fundamental result states that an NNLS design may inherently leads to sparse solutions if it satisfies the following so-called *self-regularizing* property [37].

Proposition 4: The NNLS problem (38) has a self-regularizing property if there exists a constant $\tau_{\min} > 0$ such that $\tau \geq \tau_{\min}$.

It should be noted that $\tau_{\min}$ may not be unique in general; however, Proposition 4 emphasizes the existence of such a lower bound. Accordingly, the NNLS problem (38) automatically generates a regularizing term if the condition in Proposition 4 is met. As a consequence, one can make an explicit connection between a self-regularizing NNLS design and a non-negative LASSO problem as in [37], i.e.,

$$\min_{\mathbf{d}_r \succeq \mathbf{0}} \|\mathbf{y} - \mathbf{Q}_r \mathbf{d}_r\|^2 = \min_{\mathbf{d}_r \succeq \mathbf{0}} \|\mathbf{y} - \tilde{\mathbf{Q}}_r \mathbf{d}_r\|^2 + g(\tau_{\min}) \mathbf{1}^{\mathrm{T}} \mathbf{d}_r + \mathcal{O}(\mathbf{N}^{-1/2}), \quad (40)$$

with $\tilde{\mathbf{Q}}_r = \mathbf{\Pi} \mathbf{Q}_r \mathbf{D}$, where $\mathbf{\Pi}$ is the orthogonal projection onto the subspace spanned by $\mathbf{p}$, and $\mathbf{D}$ is a diagonal matrix; see [37] for a precise proof. Further, $g(\tau_{\min}) = \tau_{\min}^2 \mathbf{1}^{\mathrm{T}} \mathbf{d}_r = \tau_{\min}^2 \|\mathbf{d}_r\|_1$ is a non-negative increasing function of $\tau_{\min}$. Therefore, the term $g(\tau_{\min}) \mathbf{1}^{\mathrm{T}} \mathbf{d}_r$ in the right-hand side of (40) can be viewed as the LASSO penalty, i.e., it behaves as a sparsity-promoting ℓ_1-norm regularization. It is well known that a larger ℓ_1-norm penalty leads to sparser optimal solutions for the (non-negative) LASSO problem. Since the regularizing multiplier $g(\tau_{\min})$ is an increasing function of $\tau_{\min}$, from the analogy provided in (40), it follows that the larger the lower bound $\tau_{\min}$, the sparser minimizer for the NNLS design (38) is achieved.

B. PERFORMANCE ANALYSIS OF THE NNLS-BASED SLP DESIGN

We consider the average transmitted power, i.e., the optimal value of the objective function (38) as a measure of the SLP performance. More precisely, we define

$$p \triangleq \mathbb{E}_t \left\{ \|\bar{\mathbf{u}}\|^2 \right\}, \quad (41)$$

implying that the SLP with a smaller p has a more favorable performance. It is important to note that the expectation in (41) is taken over symbol time t. This is due to the fact that the transmitted signal $\bar{\mathbf{u}}$ as well as some other design parameters, such as $\mathbf{A}$, $\mathbf{W}$, and $\mathbf{d}$, are all functions of the UTs' symbol vector $\mathbf{s}$, and therefore, they vary over symbol time. However, we drop the symbol time index from our notation for the brevity of notation. Furthermore, as explained in the following, p has an implicit dependence on $\mathbf{d}_r$.

Consider the reduced NNLS problem in (38) with optimal solution $\mathbf{d}_r^*$. In addition, let

$$\min_{\mathbf{d}_r} \quad \|\mathbf{y} - \mathbf{Q}_r \mathbf{d}_r\|^2$$

$$\text{s.t.} \quad d_j \geq 0, \ \forall j \in \mathbb{K},$$

$$d_j = 0, \ \forall j \notin \mathbb{K}, \tag{42}$$

be another design with minimizer $\hat{\mathbf{d}}_r^*$ and $\mathbb{K}$ denoting an arbitrary subset of $\{1, 2, \ldots, 2K\}$. Recalling that the objective function values read as the total transmitted power, it is clear that the solution to (38) is never worse than that to (42), i.e.,

$$\|\mathbf{y} - \mathbf{Q}_r \mathbf{d}_r^*\|^2 \leq \|\mathbf{y} - \mathbf{Q}_r \hat{\mathbf{d}}_r^*\|^2,$$

which is immediate from the fact that (38) is a relaxation of (42). Therefore, we conclude that the design in (38) yields lower-power solutions than those of (42). In other words, one expects a larger transmitted power if the design imposes more zero constraints on the elements of $\mathbf{d}_r$. This implies that p is a decreasing function of $\tau_{\min}$.

Based on the above discussion, as far as the solution to the SLP problem is concerned, sparsity is not favourable as it reflects reduced degrees of freedom in solving (38). It is also worth noting that as $\mathbf{d}$ becomes sparser, the optimal SLP converges to the (symbol-level) ZF precoder. In the extreme case, where $\mathbf{d} = \mathbf{0}$, the potential gain of the SLP design over the symbol-level ZF completely vanishes. Using this extreme case, a lower bound on the average transmitted power can be obtained as

$$p \geq \text{Tr}\left(\boldsymbol{\Sigma}\boldsymbol{\Gamma}^2\bar{\mathbf{H}}^\dagger\bar{\mathbf{H}}^{\dagger\mathsf{T}}\right). \tag{43}$$

The separation quantity τ, as defined in (39), depends on the matrix $\mathbf{Q}_r$, so does its positive lower bound $\tau_{\min}$, if exists. From the definition of $\mathbf{Q}_r$, it further follows that $\tau_{\min}$ is in fact a function of the two matrices $[\bar{\mathbf{H}}^\dagger]_r$ and $[\mathbf{A}^{-1}]_{r,r}$, where the latter matrix itself depends on the UTs' intended symbols $\mathbf{s}$. Note that our discussion so far applies to instantaneous realizations of $\tau_{\min}$ at a given symbol period; however, to have a more meaningful analysis of the SLP performance, long-term characteristics of $\tau_{\min}^2$ are of more concern. In particular, for a given channel realization $\mathbf{H}$, we define the *inverse regularizing function* as

$$E_t\left\{\tau_{\min}^2\right\} \triangleq f\left(\bar{\mathbf{H}}, \mathbb{X}\right), \tag{44}$$

which relates the sparsity of the SLP solution to the adopted modulation scheme. This enables us to study the power consumption performance of the SLP design for different modulation schemes and even different channel characteristics by analyzing the inverse regularizing function $f(\bar{\mathbf{H}}, \mathbb{X})$. Note that having $\tau^2 \geq \tau_{\min}^2$, we are guaranteed that $E_t\{\tau^2\} \geq E_t\{\tau_{\min}^2\}$. The following corollary concludes this subsection by providing a qualitative inverse relation between the transmitted power p and $f(\bar{\mathbf{H}}, \mathbb{X})$.

Corollary 5: Let $\tau_{\min,1}$ and $\tau_{\min,2}$ be associated with two SLP designs with two (possibly) different modulation

schemes $\mathbb{X}_1$ and $\mathbb{X}_2$, respectively. Further, let $E_t\{\tau_{\min,1}^2\} = f(\bar{\mathbf{H}}, \mathbb{X}_1)$ and $E_t\{\tau_{\min,2}^2\} = f(\bar{\mathbf{H}}, \mathbb{X}_2)$ be the regularizing functions associated with $\mathbb{X}_1$ and $\mathbb{X}_2$. Then, under identical channel realizations, $f(\bar{\mathbf{H}}, \mathbb{X}_1) \leq f(\bar{\mathbf{H}}, \mathbb{X}_2)$ implies that $p_1 \leq p_2$.

Finally, we provide an analytical measure of power efficiency by deriving an explicit expression for (44) as a function of modulation parameters. The results of this section will be used in evaluating/comparing the downlink performance with different modulation schemes.

Theorem 6: A positive lower bound on the separation quantity τ associated with the NNLS design in (38) can be found as

$$\tau^2 \geq \frac{\lambda}{2L}\left(\frac{1}{L + \sum_{l=1}^{L}\cos\phi_l}\right) \triangleq \tau_{\min}^2, \tag{45}$$

where $\lambda = \lambda_{\min}([(\bar{\mathbf{H}}\bar{\mathbf{H}}^\mathsf{T})^{-1}]_{r,r}) > 0$ with $\lambda_{\min}(\cdot)$ denoting the minimum eigenvalue.

Proof: See Appendix. ∎

Based on the lower bound in (45), the following theorem states the main result of this section by providing an approximation for the regularizing function.

Theorem 7: Given $\bar{\mathbf{H}}$ and $\mathbb{X}$, for the NNLS-based SLP design, we have

$$f(\bar{\mathbf{H}}, \mathbb{X}) \approx \frac{\lambda}{2}\left(\frac{1}{K\beta(1-\beta) + K^2\beta^2}\right)$$

$$\times \left(\frac{M_b}{M_b + \sum_{i\in\mathbf{bd}(\mathbb{X})}\cos\phi_i}\right). \tag{46}$$

where $\beta = M_b/M$.

Proof: See Appendix. ∎

In the special case, where the boundary constellation points are uniformly distributed, $\mathbf{bd}(\mathbb{X})$ is an equilateral and equiangular convex polygon (i.e., a regular polygon). For this special geometry, we have

$$\phi_i = \phi, \ \forall i \in \mathbf{bd}(\mathbb{X}), \tag{47}$$

and therefore,

$$f(\bar{\mathbf{H}}, \mathbb{X}) \approx \frac{\lambda}{2}\left(\frac{1}{K\beta(1-\beta) + K^2\beta^2}\right)\left(\frac{1}{1+\cos\phi}\right). \tag{48}$$

It should be noted that this special geometry does not make any assumption on the placement of the interior constellation points belonging to $\mathbf{int}(\mathbb{X})$. The condition specified by (47) is met by constellation sets of some well-known modulation schemes, e.g., PSK and APSK. In the particular case of PSK modulations with uniformly-distributed boundary symbols, since the constellation has no interior points, we have $\beta = 1$, which yields

$$f(\bar{\mathbf{H}}, \mathbb{X}) \approx \frac{\lambda}{2K^2}\left(\frac{1}{1+\cos\phi}\right). \tag{49}$$

It can be seen from (48) that the regularizing function $f(\bar{\mathbf{H}}, \mathbb{X})$ does not depend on the exact locations of the constellation

symbols but only on the relative angular positioning of the symbols (this latter specification is reflected in the shape of distance-preserving CIRs). Based on (48), the same statement holds true for the SLP's performance, completing the proof of Theorem 3.

VI. SIMULATION RESULTS

In this section, we provide some simulation results to verify our analytical discussions in the earlier sections. In particular, we aim to verify via simulation results that the performance of different precoding techniques of interest, i.e., MMSE, ZF, and SLP, is invariant to the differential phase estimation process at the receiver but the system performance is affected by the phase noise at the transponder LOs. Even if the problem formulation for these precoding techniques are different, ZF and MMSE formulation are power constraint problems, while the SLP method analyzed considers the power minimization with quality of service (QoS) constraints, this work is mainly focused on the constructive interference constraints in the SLP design problem and on how they are affected by phase uncertainty. This appears with the same formulation in both power minimization and QoS-constrained SLP problems. Besides, as shown in [36], the SLP power minimization problem solution for PSK modulations is sub-optimal for the QoS-constrained SLP problem under proper power scaling. For this reason, we considered equal transmit power for all the precoding schemes in our simulations. More specifically, we normalized the SLP power minimization problem solution so that the precoded vector has the same power as the ZF and MMSE precoding schemes.

To analyze the results we focus on three performance metrics: spectral efficiency, symbol error rate (SER), and receive SNIR. We calculate the spectral efficiency as the ratio of the product of the average UEs' bit error rate (BER) and the per-user achievable rate divided by the total consumed power. Due to the lack of closed-form expressions for SLP, we use empirical probability distributions obtained over sufficiently many independent realizations of the channel and the users' symbols to approximate the mutual information for each user, as done in [38]. The SER is calculated as the ratio of the number of symbols received with errors of the total number of transmitted symbols. Finally, the SNIR is defined as the ratio of the received signal's power over the interference plus noise power at the receivers.

The simulation setup considered a downlink MU-MISO system with multiuser precoding, where independent data symbols are intended for the UTs. At the UTs, identical noise distributions $z_k \sim \mathcal{CN}(0, \sigma^2)$ with $\sigma^2 = 1$ are assumed, for all $k = 1, \ldots, K$. Independent Rayleigh block fading channels are further assumed between each transmitter-UT antenna pair, where IID realizations $\{\mathbf{h}_k\}_{k=1}^K$ are randomly generated for each fading block from the standard circularly symmetric complex Gaussian distribution, i.e., $\mathbf{h}_k \sim \mathcal{CN}(\mathbf{0}, \mathbf{I})$. The use of this channel model is fundamented by the intention to prove the performance of the precoding method is invariant to the

differential phase estimation process at the receiver for any communication scenario, terrestrial o satellite.

Fig. 5(a) represents the simulation diagram of this experiment. As can be appreciated in the figure, the signal for each beam is the concatenation done at the "Multiplexer" block of the non-precoded pilots and the precoded data. The formers are BPSK-modulated Walsh-Hadamard sequences, precisely predefined and fixed for each beam. For the modulation of the payload data, we evaluate two alternatives, QPSK and 8PSK. In the linear precoding techniques, the payload data is multiplied by the precoding matrix after being modulated. The precoding matrix is calculated by the "Linear Precoding" block, considering the linear precoding techniques mentioned before. However, as mentioned in previous sections, the SLP method directly calculates the precoded transmit signal on a symbol-by-symbol basis. For that reason, the "M-PSK Modulator," the mixers, and the "Linear Precoding" blocks in 5(a) are replaced by a "SLP" block that calculates the precoded symbols for each beam. These modifications are represented in Fig. 5(b). In both simulation diagrams, the "Channel Matrix" block introduces the interbeam interference and the independent additive noise at the receivers, as described by (1).

The block "PLL" is essential in any practical implementation to acquire and track the phase of the received signal. However, it makes all the phases measured at the UTs relative to the phase of the intended beams. In this simulation, we compare the performance of the system for an ideal "PLL" block which can obtain the absolute phase measurement against the actual "PLL" block.

The block "CSI Estimation" estimates the channel matrix as the correlation between the received signal and the expected non-precoded pilot for each beam. In this way, each UT can estimate the channels from each beam. These estimations are the input of the "Linear Precoding" and the "SLP" blocks. Meanwhile, the precoded payload data is demodulated and used to calculate the different performance metrics. The simulation is run under a set of signal-to-noise ratio (SNR) $E_s/N_0 = \{-10, \ldots, 30\}$ dB and the results are the average of all the UTs' performance for each instance of E_s/N_0. The SNR is defined as the ratio of the average power received over the receiver additive white Gaussian noise (AWGN).

Fig. 6 shows a comparison using the spectral efficiency as a metric to evaluate the performance of an ideal system, where the PLL can obtain absolute phase measurements at the UT against the realistic system, with relative phase measurements. As can be appreciated in the figure, there is no difference between both results for QPSK or 8PSK signaling with any of the precoding techniques evaluated. The equivalent results for SER and SNIR metrics are shown in Figs. 7 and 8, respectively. For these metrics, there is also no difference between the ideal and the actual system for any evaluated modulation or precoding techniques.

In addition, we designed another set of experiments to verify that the system performance is affected by the hardware impairments at the transponder. Similar to the previous
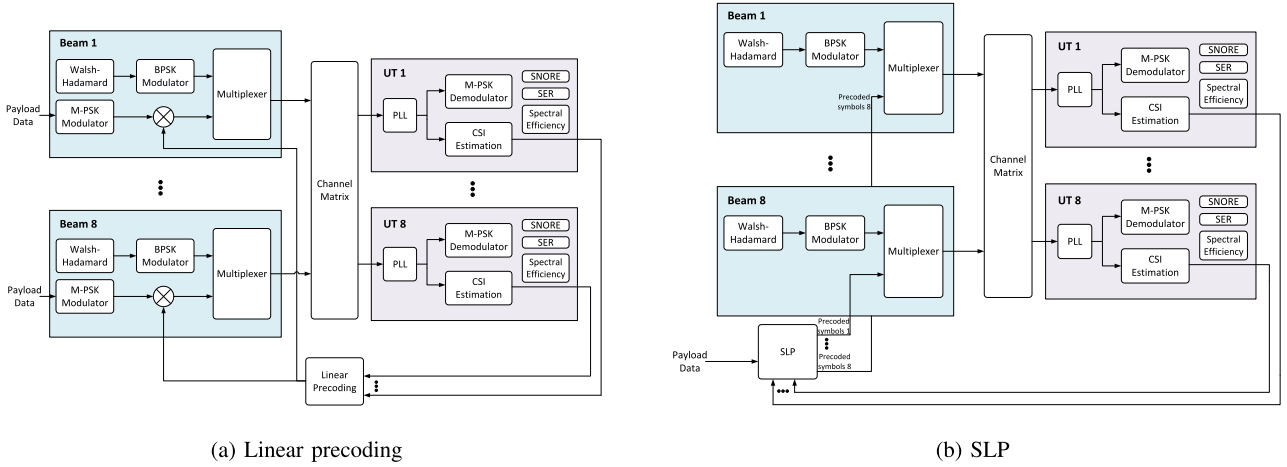
(a) Linear precoding   (b) SLP

FIGURE 5. Simulation diagram for the experiment to verify that the performance of different precoding techniques is invariant to the differential phase estimation process at the UTs.
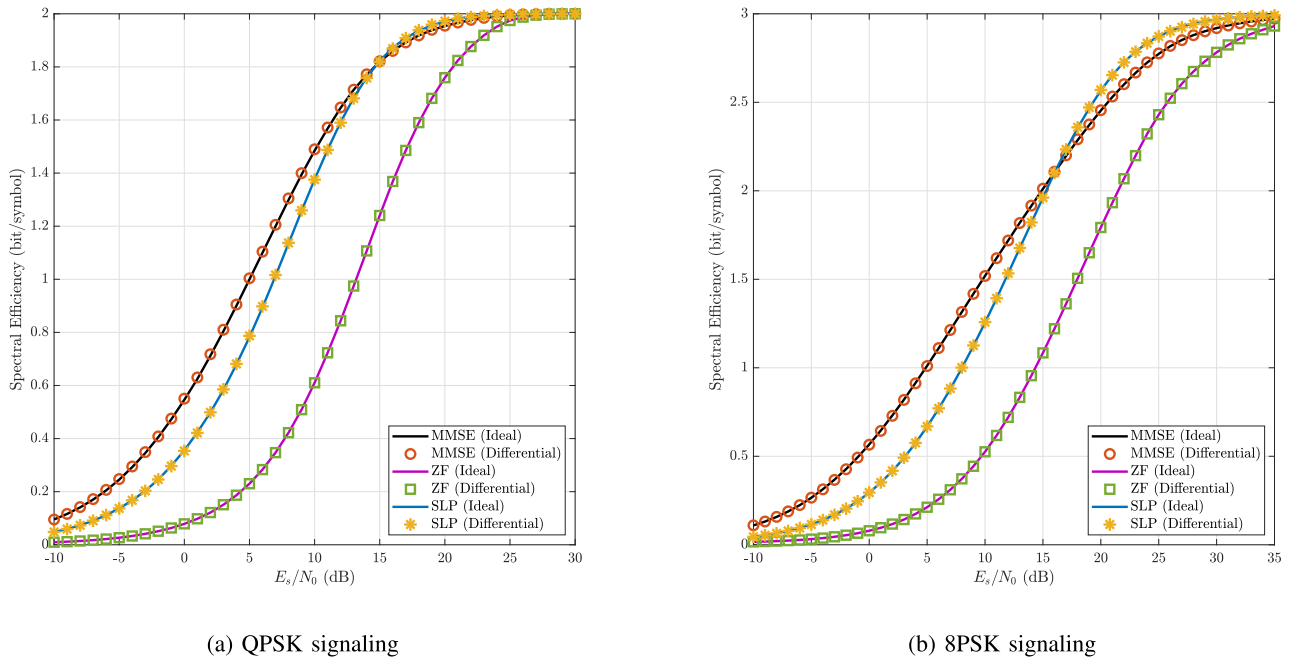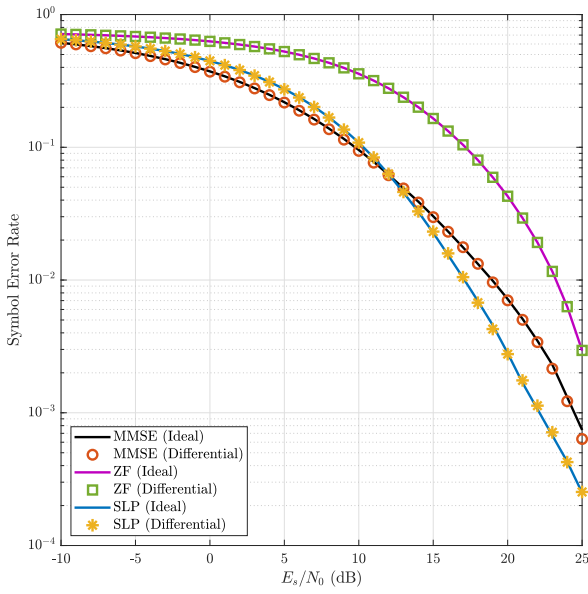

(a) QPSK signaling   (b) 8PSK signaling

FIGURE 6. Spectral efficiency comparison of different precoding techniques with ideal and differential phase estimation for $N = K = 8$.

simulations, we used the spectral efficiency, the SER, and the receive SNIR as performance metrics under the simulation setup previously described. The simulation diagram is represented in Fig. 9, which is very similar to the previous setup except for the removed "PLL" block, the "Frequency Reference" and eight "LOs" blocks that were added at the transponder. Considering the results of the previous simulations and for the sake of simplicity, we used ideal "PLLs" for this experiment, which are not represented in Fig. 9. On the other hand, we included the "Frequency Reference" and the "LOs" blocks to emulate the phase noise of the transponder's LO. In this experiment, we consider the best possible configuration in synchronization terms, using a single frequency

reference to transmit all the beams. Another modification of this simulation setup with respect to the previous one is the channel model considered for this experiment, which is the flat fading model typically used in GEO satellite systems.

We considered an ideal LO at the gateway and three different options for the frequency reference at the transponder: a very stable crystal oscillator with Allan variance $\sigma_y^2(0.5) = 0.232$, a medium-class ($\sigma_y^2(0.5) = 2.321$), and an economic crystal oscillator ($\sigma_y^2(0.5) = 23.208$), all with nominal frequency $f_0 = 10\,\text{MHz}$. The value $\tau = 0.5$ in the Allan variance is related to the loop delay (0.5 s), which considers the feedback link from the UTs to the gateway through the GEO satellite. Fig. 9 represents the simulation diagram for linear
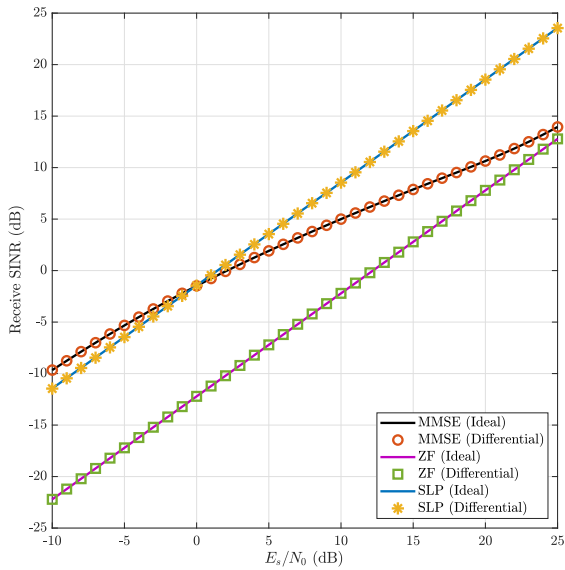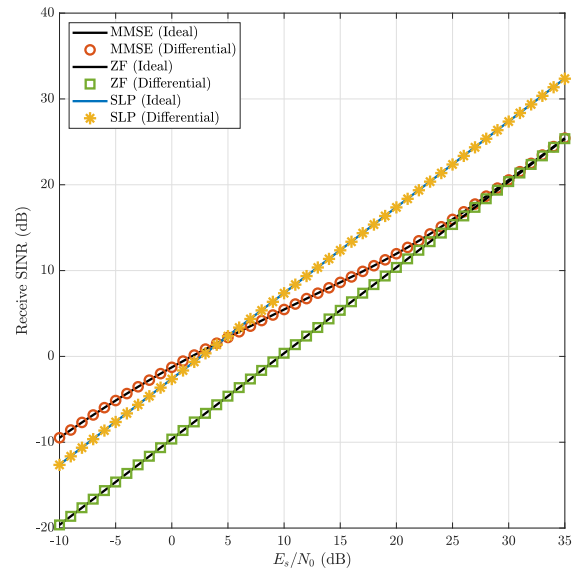
(a) QPSK signaling
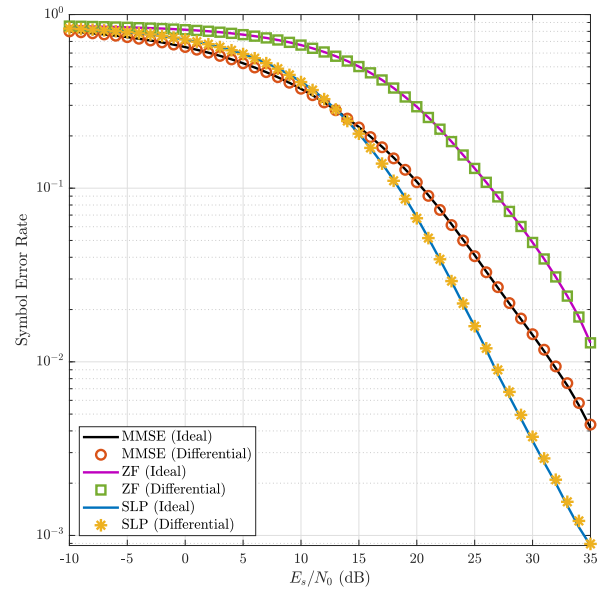
(b) 8PSK signaling

FIGURE 7. Average SER performance of different precoding techniques per UT with ideal and differential phase estimation for $N = K = 8$.

(a) QPSK signaling

(b) 8PSK signaling

FIGURE 8. Average receive SNIR of different precoding techniques per UT with ideal and differential phase estimation for $N = K = 8$.

precoding methods, the equivalent diagram for SLP is not included for the sake of space. However, both experiments (Figs. 5 and 9) analyzed the same precoding techniques: ZF, MMSE, and SLP.

The phase noise was generated using the two-state model described in [39]. We considered eight uplink-forward carrier frequencies between $f_{U_1} = 47.5$ GHz and $f_{U_8} = 48.9$ GHz with 200 MHz bandwidth each. The downlink-forward carrier frequency, common to all the beams using precoding,

was 20 GHz. The PSD of the phase noise obtained for these parameters is represented in Fig. 10. As it can be appreciated in the figure, the difference between the PSD of each beam for the same frequency reference is small. However, even this small difference can affect the precoding performance, as we can see in figures Figs. 11 to 13.

Figs. 11 to 13 show the results of the simulations to evaluate the effects of the phase noise at the transponder LOs for the different metrics: Fig. 11 shows the receiver SNIR, Fig. 12
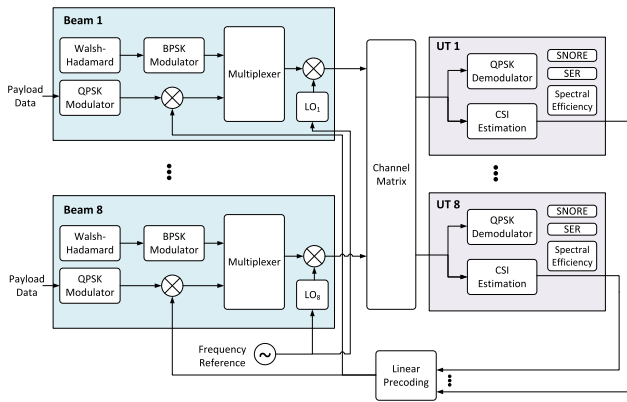
FIGURE 9. Simulation diagram for the experiment to verify that the system performance is affected by the phase noise at the transponder LOs.
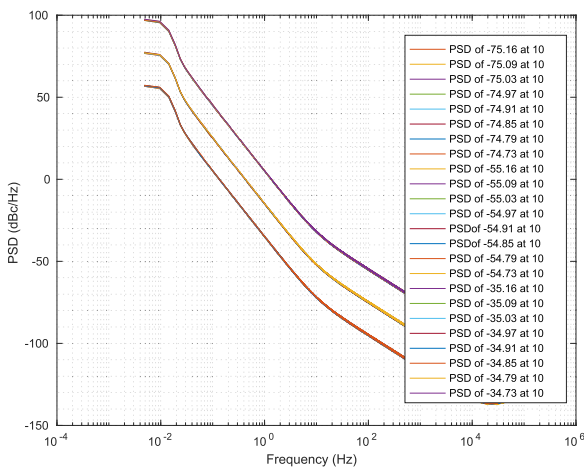

FIGURE 10. PSD of the phase noise at each of the eight beams for the three frequency references considered in the simulations: high quality ($\sigma_\gamma^2(0.5) = 0.232$), medium-class ($\sigma_\gamma^2(0.5) = 2.321$) and economic crystal oscillator ($\sigma_\gamma^2(0.5) = 23.208$).

the SER and Fig. 13 the spectrum efficiency. In these figures, the ideal curves represent the case with a perfect frequency reference without phase noise (PN) at the transponder, which means that the "Frequency Reference" and the "LOs" blocks do not add any phase rotation to the signal. The (No FDM) curves represent the case of a realistic frequency reference with PN and ideal uplink transmission without FDM. This implies that a phase variation from the "Frequency Reference" is added to the signal, but in this case, it is constant for all the beams, *i.e.*, the "LOs" blocks have the same value for all the beams. The solid curves represent the realistic case, where the frequency reference has PN, and the uplink transmission uses different carrier frequencies for each beam's datastream, in other words, FDM. In this case, the phase noise added to each beam is generated by the "LOs" blocks considering the "Frequency Reference" phase noise PSD represented in Fig. 10.
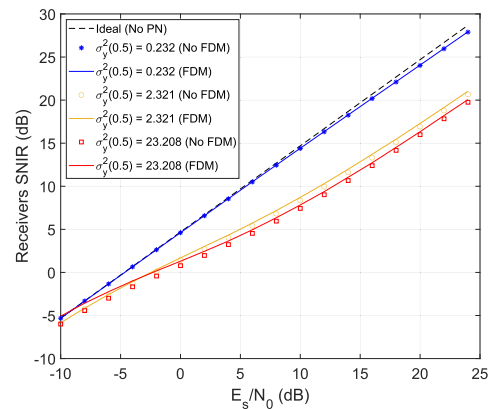
As it can be appreciated in Fig. 11, for the same frequency reference, the receiver SNIR is more affected in SLP,
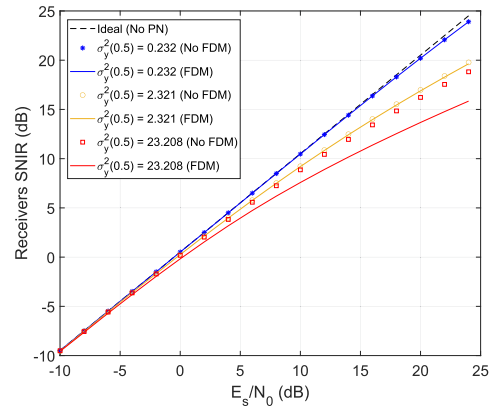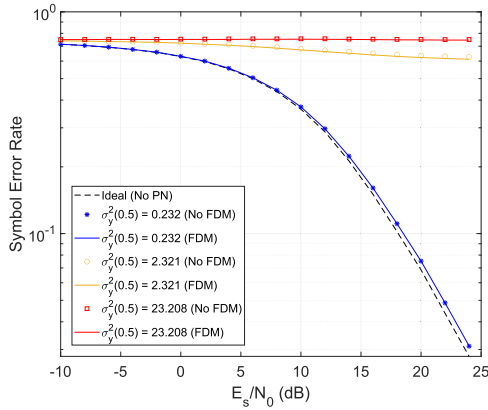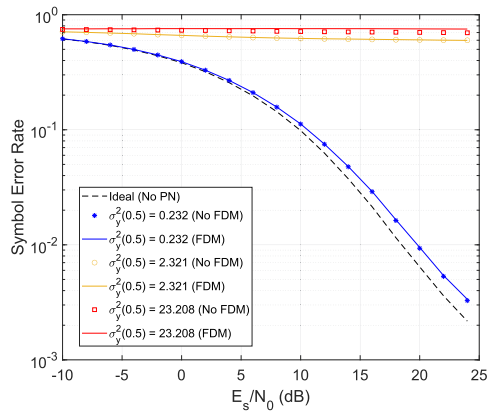

(a) ZF precoding
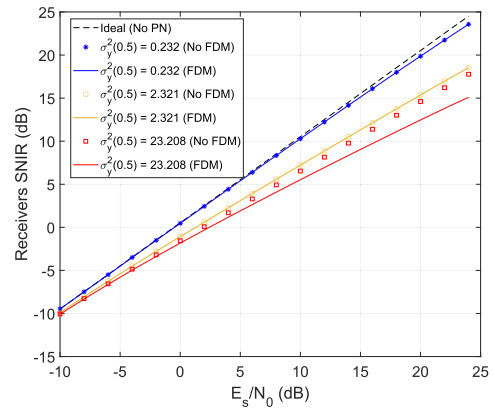
(b) MMSE precoding

(c) SLP precoding

FIGURE 11. Comparison of the average SNIR at the UTs for $N = K = 8$, and QPSK signaling for three different frequency references: a very stable (Allan variance $\sigma_\gamma^2(0.5) = 0.232$), a medium-class ($\sigma_\gamma^2(0.5) = 2.321$) and an economic crystal oscillator ($\sigma_\gamma^2(0.5) = 23.208$).

Fig. 11(c) than in linear precoding systems, Fig. 11(a) and (b). For instance, for linear precoding techniques with $E_s/N_0 = 0$ dB, the receivers SNIR degradation concerning the expected value without considering the hardware impairments is less than 1 dB for medium-class frequency references: 1.55 dB for MMSE and 0.26 dB for ZF while the equivalent value
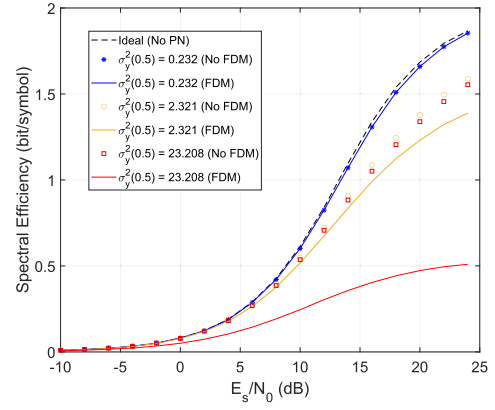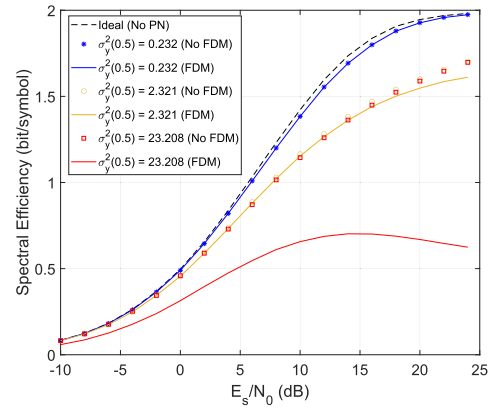
(a) ZF precoding

(b) MMSE precoding
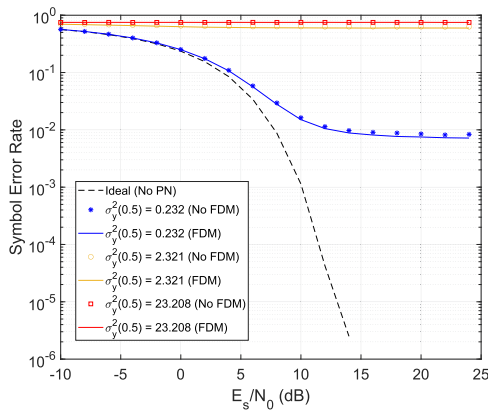
(c) SLP precoding

FIGURE 12. Average SER comparison for $N = K = 8$ and QPSK signaling for three different frequency references: a very stable (Allan variance $\sigma_y^2(0.5) = 0.232$), a medium-class ($\sigma_y^2(0.5) = 2.321$) and an economic crystal oscillator ($\sigma_y^2(0.5) = 23.208$).

(a) ZF precoding

(b) MMSE precoding

(c) SLP precoding

FIGURE 13. Spectral efficiency comparison for $N = K = 8$ and QPSK signaling for three different frequency references: a very stable (Allan variance $\sigma_y^2(0.5) = 0.232$), a medium-class ($\sigma_y^2(0.5) = 2.321$) and an economic crystal oscillator ($\sigma_y^2(0.5) = 23.208$).
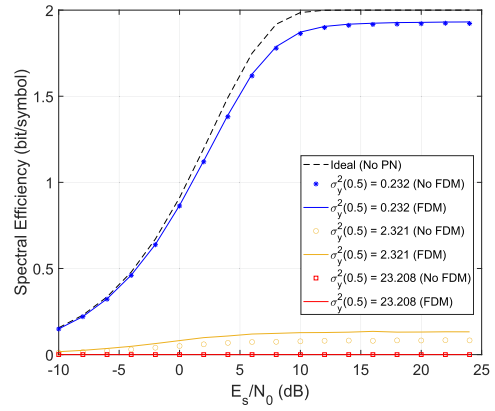
for SLP is 2.93 dB. However, according to the receivers SNIR metric, the performance of the system is barely affected when high-quality frequency references ($\sigma_y^2(0.5) = 0.232$) are used; see the blue curves in Fig. 11. Besides, the performance degradation is stronger for high SNR values. It can be up to 8.66 dB for ZF, 9.42 dB (MMSE), and 8.63 dB

(SLP) at $E_s/N_0 = 25$ dB, where the inter-beam interference is stronger.

On the other hand, for the SER comparison, the transponder phase noise's effects are more evident in SLP than in linear precoding methods. Specifically for $E_s/N_0 \geq 5$ dB, the SER of the system using SLP degrades significantly. This can be

corroborated in Fig. 12(c), where the blue curve moves away from the ideal one and stays constant for $E_s/N_0 \geq 15$ dB. However, even with performance degradation related to the hardware implementation's phase uncertainties, the SER of SLP outperform the SER of linear precoding systems for SNR values under 20 dB ($E_s/N_0 \leq 20$ dB). Besides, as it can be appreciated in the figures, the SER deteriorates considerably for the medium and economic frequency references independently of the precoding technique considered.

Similar to the previous comparisons, the spectral efficiency analysis (Fig. 13) shows that linear precoding systems are more resilient to the hardware implementation's phase uncertainties than SLP. In this case, the spectral efficiency of the system using a medium-class frequency reference ($\sigma_y^2(0.5) = 2.321$) is strongly degraded for SLP, which can be corroborated by analyzing the separation between the ideal (dashed black) and the realistic (solid yellow) curves in Fig. 13(c). However, for high-quality frequency references ($\sigma_y^2(0.5) = 0.232$), the spectral efficiency of SLP systems is much better than linear precoding ones.

Analyzing the simulation results considered during this section, we can arrive at some conclusions:

- In general, SLP outperforms ZF and MMSE for high E_s/N_0 scenarios.
- For low values of E_s/N_0, the performance of SLP and MMSE is very similar and superior to ZF performance.
- The E_s/N_0 threshold value where SLP outperforms MMSE increases with the modulation order.
- The expected system performance for precoding-enabled satellite communication systems considerably degrades when the phase noise of the transponder's LO is included in the analysis. Even for the optimal synchronization configuration and the typical frequency reference ($\sigma_y^2(0.5) = 2.321$).
- Although linear precoding techniques are more resilient to the hardware impairments inherent to satellite communication systems than SLP, the system's performance using high-quality frequency reference is better for SLP than linear precoding techniques.

VII. CONCLUSION

Linear and symbol-level precoding in satellite communications have received increasing research attention thanks to its capacity to solve the problem of inter-beam interference by applying a full frequency reuse approach. However, there are still challenges and open questions for the practical implementation of precoding systems. Some examples of this are the inability to measure the absolute phase offset induced by the propagation channel and the phase uncertainties related to using FDM in the forward uplink.

This article addressed the impact of these phase variations and uncertainties in operating a precoded forward link satellite communication system. It formally demonstrated that the phase uncertainties created in the forward downlink do not affect the precoding performance for linear and non-linear precoding operations. This result was validated using three

performance metrics: spectral efficiency, SER, and receivers SNIR, in a downlink MU-MISO system with eight beams and an equal number of UTs. The precoding schemes analyzed were MMSE, ZF, and DPCIR-based SLP.

Additionally, it was shown that the UTs could estimate the phase variations related to the transponder LOs as part of the CSI. The effect of this impairment is determined by the phase noise of the LOs' frequency reference at the transponder and the delay of the precoding loop. Our simulations used an 8x8 MU-MISO precoding system to compare the impact of three different frequency references for linear and non-linear precoding methods. The simulations assumed a GEO satellite transponder where all the LOs shared a single frequency reference, which is the optimal scenario from a synchronization point of view. If this assumption does not hold, for instance, if the LOs use different frequency references or in distributed satellite systems, the performance degradation shown in our simulations will be more substantial. In addition, the effects of the Doppler shift in the feeder link will affect each FDM carrier differently depending on its center frequency, increasing the performance degradation shown. Therefore, our simulation results provide an upper bound for the precoding performance in GEO satellite systems.

Analyzing the simulation results included in this work, we can conclude that, in general, SLP outperforms ZF and MMSE for high E_s/N_0 scenarios. On the other hand, for lower values of E_s/N_0, the slight difference between SLP and MMSE performance may not justify the high complexity of SLP implementation. According to our simulation results, the E_s/N_0 threshold value where SLP outperforms MMSE increases with the modulation order. However, we can see that SLP is more affected by the hardware impairments inherent to satellite communication systems. For instance, according to our simulation results, the performance of a system with a high-quality crystal oscillator ($\sigma_y^2(0.5) = 2.321$), and SLP differs considerably from the ideal scenario, without the phase uncertainties inherent to hardware implementations. However, it is better than the performance of the equivalent system using linear precoding techniques.

Finally, the authors would like to highlight that the main contribution of this work is the formal demonstration of the accurate performance of the precoding technique, which is not affected by the phase uncertainties in the forward downlink. Another significant result of this study is the conclusion that using a common frequency reference to process all the beams at the transponder does not avoid the phase uncertainties related to the FDM in the forward uplink. This fact has to be considered to set the expected performance of practical implementations of MU-MISO precoding systems where a differential phase compensation loop should be included to compensate for this performance degradation.

The phase compensation loop can be designed similarly to a distributed PLL, where the compensation is calculated using the inter-beam differential phase estimated at the user terminals as input. This solution, similar to the algorithms implemented in [4] and [5] for distributed satellite systems,

is based on the working principle of PLLs: To calculate a phase output such that the difference between output and input phases is minimum. In our case, one of the beams is considered the reference, and the PLL phase output or compensation is applied to the other beams to keep the differential phases between them and the reference beam constant.

APPENDIX

A. PROOF OF THEOREM 6

We start from the definition of $\mathbf{Q}_r$ by recalling that

$$\mathbf{Q}_r^T \mathbf{Q}_r = [\mathbf{A}^{-1}]_{r,r}^T [\bar{\mathbf{H}}^\dagger]_r^T [\bar{\mathbf{H}}^\dagger]_r [\mathbf{A}^{-1}]_{r,r} \quad (50)$$

Therefore, we can obtain

$$\mathbf{p}^T \mathbf{Q}_r^T \mathbf{Q}_r \, \mathbf{p} \geq \lambda_{\min}\left([\bar{\mathbf{H}}^\dagger]_r^T [\bar{\mathbf{H}}^\dagger]_r\right)$$
$$\times \mathbf{p}^T [\mathbf{A}^{-1}]_{r,r}^T [\mathbf{A}^{-1}]_{r,r} \, \mathbf{p}, \quad (51)$$

where $\lambda_{\min}(\cdot)$ denotes the maximum eigenvalue. In addition,

$$\lambda_{\min}\left([\bar{\mathbf{H}}^\dagger]_r^T [\bar{\mathbf{H}}^\dagger]_r\right) = \lambda_{\min}\left([\bar{\mathbf{H}}^{\dagger T} \bar{\mathbf{H}}^\dagger]_{r,r}\right)$$
$$= \lambda_{\min}\left([(\bar{\mathbf{H}}\bar{\mathbf{H}}^T)^{-1}]_{r,r}\right) \triangleq \lambda. \quad (52)$$

Since $\bar{\mathbf{H}}$ is full column rank, it follows that $\bar{\mathbf{H}}^T\bar{\mathbf{H}} \succ 0$, and hence $(\bar{\mathbf{H}}\bar{\mathbf{H}}^T)^{-1} \succ 0$. Due to the fact that removing rows and columns of a matrix does not affect its positive/negative definiteness, we further conclude that $[(\bar{\mathbf{H}}\bar{\mathbf{H}}^T)^{-1}]_{r,r} \succ 0$, and thus, all its eigenvalues, including the minimum one, are positive. Therefore, we always have $\lambda > 0$. Consequently, using (51), we can obtain a lower bound on τ^2 as

$$\tau^2 = \min_{\mathbf{p} \in \mathcal{S}^{2L-1}} \frac{1}{2L} \mathbf{p}^T \mathbf{Q}_r^T \mathbf{Q}_r \, \mathbf{p}$$

$$\geq \min_{\mathbf{p} \in \mathcal{S}^{2L-1}} \frac{\lambda}{2L} \mathbf{p}^T [\mathbf{A}^{-1}]_{r,r}^T [\mathbf{A}^{-1}]_{r,r} \, \mathbf{p}$$

$$= \min_{\mathbf{p} \in \mathcal{S}^{2L-1}} \frac{\lambda}{2L} \mathbf{p}^T [\mathbf{A}^{-T} \mathbf{A}^{-1}]_{r,r} \, \mathbf{p}, \quad (53)$$

where the last equality can easily be verified by exploiting the block-diagonal structure of $\mathbf{A}$. In order to derive an explicit expression for the lower bound in (53), one needs to solve the following constrained minimization problem:

$$\mathcal{P}1 : \quad \min_{\mathbf{p} \in \mathcal{S}^{2L-1}} \quad \mathbf{p}^T [(\mathbf{A}\mathbf{A}^T)^{-1}]_{r,r} \, \mathbf{p}. \quad (54)$$

Using the definition of $\mathcal{S}^{2L-1}$, the problem $\mathcal{P}1$ can be rewritten as

$$\mathcal{P}1 : \quad \min_{\mathbf{p}} \quad \mathbf{p}^T [(\mathbf{A}\mathbf{A}^T)^{-1}]_{r,r} \, \mathbf{p}$$

$$\text{s.t.} \quad \mathbf{p}^T \mathbf{1} = \mathbf{1}$$

$$\mathbf{p} \succeq \mathbf{0}. \quad (55)$$

Let us first consider a relaxation of (55) by ignoring the non-negativity constraints, i.e.,

$$\mathcal{P}2 : \quad \min_{\mathbf{p}} \quad \mathbf{p}^T [(\mathbf{A}\mathbf{A}^T)^{-1}]_{r,r} \, \mathbf{p}$$

$$\text{s.t.} \quad \mathbf{p}^T \mathbf{1} = \mathbf{1} \quad (56)$$

Since the matrix $\mathbf{A}$ has a block-diagonal structure, we can write $\mathbf{A}\mathbf{A}^T = \text{blkdiag}(\mathbf{A}_1\mathbf{A}_1^T, \dots, \mathbf{A}_K\mathbf{A}_K^T)$. Accordingly, $(\mathbf{A}\mathbf{A}^T)^{-1} = \text{blkdiag}((\mathbf{A}_1\mathbf{A}_1^T)^{-1}, \dots, (\mathbf{A}_K\mathbf{A}_K^T)^{-1})$, and thus

$$[(\mathbf{A}\mathbf{A}^T)^{-1}]_{r,r} = \text{blkdiag}\left((\mathbf{A}_1\mathbf{A}_1^T)^{-1}, \dots, (\mathbf{A}_L\mathbf{A}_L^T)^{-1}\right). \quad (57)$$

Similarly, we can partition $\mathbf{p}$ as $\mathbf{p} = [\mathbf{p}_1, \dots, \mathbf{p}_L]^T$ such that for any $l \in \{1, \dots, L\}$, $\mathbf{p}_l \in \mathbb{R}^2$ corresponds to the block $\mathbf{A}_l \mathbf{A}_l^T$ in $\mathbf{A}\mathbf{A}^T$. As a result, the problem $\mathcal{P}2$ can be recast as

$$\mathcal{P}2 : \quad \min_{\{\mathbf{p}_l\}_{l=1}^L} \quad \sum_{l=1}^{L} \mathbf{p}_l^T (\mathbf{A}_l \, \mathbf{A}_l^T)^{-1} \, \mathbf{p}_l$$

$$\text{s.t.} \quad \mathbf{1}^T \sum_{l=1}^{L} \mathbf{p}_l = 1 \quad (58)$$

Applying the method of Lagrange multipliers, we can obtain the Lagrangian of (58) as

$$\mathcal{L}(\mathbf{p}_1, \dots, \mathbf{p}_L, \mu) = \sum_{l=1}^{L} \mathbf{p}_l^T (\mathbf{A}_l \, \mathbf{A}_l^T)^{-1} \mathbf{p}_l + \mu \left(\mathbf{1}^T \sum_{l=1}^{L} \mathbf{p}_l - 1\right), \quad (59)$$

where μ denotes the Lagrange multiplier. From (59), by taking partial derivative with respect to $\mathbf{p}_l$, it follows that

$$\frac{\partial \mathcal{L}(\mathbf{p}_1, \dots, \mathbf{p}_L, \mu)}{\partial \mathbf{p}_l} = 2(\mathbf{A}_l \, \mathbf{A}_l^T)^{-1} \mathbf{p}_l + \mu \, \mathbf{1}, \quad (60)$$

Equating (60) to zero, we obtain

$$\mathbf{p}_l^* = -\frac{1}{2} \mu^* \, \mathbf{A}_l \, \mathbf{A}_l^T \mathbf{1}, \quad (61)$$

Substituting (61) for $\mathbf{p}_l$ in the constraint of $\mathcal{P}2$ results in

$$1 = -\frac{1}{2} \mathbf{1}^T \sum_{l=1}^{L} \mu^* \, \mathbf{A}_l \, \mathbf{A}_l^T \mathbf{1}$$

$$= -\frac{1}{2} \mu^* \sum_{l=1}^{L} \mathbf{1}^T \mathbf{A}_l \, \mathbf{A}_l^T \mathbf{1}$$

$$= -\mu^* \sum_{l=1}^{L} 1 + \cos\phi_l, \quad (62)$$

From (62), we obtain

$$\mu^* = \frac{-1}{\sum_{l=1}^{L} 1 + \cos\phi_l} \quad (63)$$

By replacing μ^* in (61), the optimal solution to $\mathcal{P}2$ is obtained by

$$\mathbf{p}_l^* = \frac{1 + \cos\phi_l}{2 \sum_{l=1}^{L} 1 + \cos\phi_l} \, \mathbf{1}, \quad (64)$$

It is immediate from (64) that $\mathbf{p}_l^* \succeq \mathbf{0}$ for all $l = 1, 2, \dots, L$. Therefore, $\mathbf{p}^* = [\mathbf{p}_1^*, \dots, \mathbf{p}_L^*]^T$ is also a feasible (and clearly the optimal) solution to the problem $\mathcal{P}1$. Thus, problems $\mathcal{P}1$ and $\mathcal{P}2$ are equivalent. The optimum of $\mathcal{P}1$ can then be computed by substituting (64) in the objective function of $\mathcal{P}2$,

which yields

$$\sum_{l=1}^{L} \mathbf{p}_l^{*T} (\mathbf{A}_l \, \mathbf{A}_l^{T})^{-1} \, \mathbf{p}_l^{*} = \frac{1}{2} \left(\frac{1}{L + \sum_{l=1}^{L} \cos \phi_l} \right). \qquad (65)$$

Finally, plugging (65) into (53), gives the following positive lower bound on τ^2:

$$\tau^2 \geq \frac{\lambda}{2L} \left(\frac{1}{L + \sum_{l=1}^{L} \cos \phi_l} \right) \triangleq \tau_{\min}^2. \qquad (66)$$

B. PROOF OF THEOREM 7

Using the lower bound $\tau_{\min}^2$ provided in (66), the regularizing function can be evaluated as

$$f(\bar{\mathbf{H}}, \mathbb{X}) = \frac{\lambda}{2} \, \mathrm{E} \left\{ \frac{1}{L^2 + L \sum_{l=1}^{L} \cos \phi_l} \right\}. \qquad (67)$$

The reciprocal form of the expectation's argument in (67) is non-linear in both L and $\cos \phi_l$, which makes the expectation computationally intractable. Denoting $\Phi \triangleq L^2 + L \sum_{l=1}^{L} \cos \phi_l$ and using the Taylor expansion of $\mathrm{E}\{1/\Phi\}$ around $\mathrm{E}\{\Phi\}$, we can obtain an approximation for the regularizing function as

$$f(\bar{\mathbf{H}}, \mathbb{X}) \approx \frac{\lambda}{2} \left(\frac{1}{\mathrm{E}\{\Phi\}} + \mathcal{O} \left(\frac{1}{\mathrm{E}\{\Phi\}^3} \right) \right). \qquad (68)$$

Next, we can write $\mathrm{E}\{\Phi\}$ as

$$\mathrm{E}\{\Phi\} = \mathrm{E}\left\{L^2\right\} + \mathrm{E}\left\{L \sum_{l=1}^{L} \cos \phi_l\right\} \qquad (69)$$

Recall that L is a binomial random process with a success rate $M_{\mathrm{b}}/M \triangleq \beta$ over a total number of K trials. Hence $\mathrm{E}\{L\} = K\beta$, $\mathrm{Var}\{L\} = K\beta(1-\beta)$, and $\mathrm{E}\{L^2\} = K\beta(1-\beta) + K^2\beta^2$. On the other hand, the second expectation in the right-hand side of (69) is obtained as

$$\mathrm{E}\left\{L \sum_{l=1}^{L} \cos \phi_l\right\}$$

$$= \sum_{j=0}^{K} \mathrm{E}\left\{L \sum_{l=1}^{L} \cos \phi_l \bigg| L = j\right\} \Pr\{L = j; K, \beta\}$$

$$= \sum_{j=0}^{K} \mathrm{E}\left\{j \sum_{l=1}^{j} \cos \phi_l\right\} \Pr\{L = j; K, \beta\}$$

$$= \mathrm{E}\left\{\cos \phi_l\right\} \sum_{j=0}^{K} j^2 \Pr\{L = j; K, \beta\}$$

$$= \mathrm{E}\left\{\cos \phi_l\right\} \left(K\beta(1-\beta) + K^2\beta^2\right) \qquad (70)$$

Consequently,

$$\mathrm{E}\{\Phi\} = \left(K\beta(1-\beta) + K^2\beta^2\right) (1 + \mathrm{E}\left\{\cos \phi_l\right\}) \qquad (71)$$

Due to the fact that $\mathrm{E}\{\Phi\}^3 \approx \mathcal{O}(K^6)$, for moderately large values of K, it follows from (68) and (71) that

$$f(\bar{\mathbf{H}}, \mathbb{X}) \approx \frac{\lambda}{2} \left(\frac{1}{\mathrm{E}\{\Phi\}} \right)$$

$$= \frac{\lambda}{2} \left(\frac{1}{\left(K\beta(1-\beta) + K^2\beta^2\right)} \right) \left(\frac{1}{1 + \mathrm{E}\{\cos \phi_l\}} \right). \qquad (72)$$

It is worth noting that Φ is strictly positive on $[0, \pi)$. Thus $1/\Phi$ is strictly convex in the given interval. As a result, based on Jensen's inequality, we have $\mathrm{E}\{1/\Phi\} \geq 1/\mathrm{E}\{\Phi\}$, which means that the approximation in (72) is specifically a lower bound on $f(\bar{\mathbf{H}}, \mathbb{X})$.

We further remark that the expectation $\mathrm{E}\{\cos \phi_l\}$ must be taken over symbol time. However, for a sufficiently large number of symbol periods, by a direct application of the law of large numbers, this expectation can equally be taken over the constellation $\mathbb{X}$, i.e.,

$$\mathrm{E}\{\cos \phi_l\} = \frac{1}{M_{\mathrm{b}}} \sum_{i \in \mathbf{bd}(\mathbb{X})} \cos \phi_i. \qquad (73)$$

Replacing the expectation (73) in (72) yields the expression provided in Theorem 7.

REFERENCES

[1] E. Perahia and R. Stacey, *Next Generation Wireless LANs: 802.11 N and 802.11 Ac*. Cambridge, U.K.: Cambridge Univ. Press, 2013.

[2] L. T. Berger, A. Schwager, P. Pagani, and D. M. Schneider, "MIMO line communications," *IEEE Commun. Surv. Tut.*, vol. 17, no. 1, pp. 106–124, Jan.–Mar. 2015.

[3] ETSI. "Digital video broadcasting (DVB); implementation guidelines for the second generation system for broadcasting, interactive services, news gathering and other broadband satellite applications; Part 1: DVB-S2.," Tech. Rep. ETSI TR 102 376-1, 2015.

[4] K.-U. Storek, R. T. Schwarz, and A. Knopp, "Multi-satellite multi-user MIMO precoding: Testbed and field trial," in *Proc. IEEE Int. Conf. Commun.*, 2020, pp. 1–7.

[5] J. Krivochiza et al., "End-to-end precoding validation over a live GEO satellite forward link," *IEEE Access*, 2021, vol. 4, pp. 1–10.

[6] M. Á. Vázquez et al., "Precoding in multibeam satellite communications: Present and future challenges," *IEEE Wireless Commun.*, vol. 23, no. 6, pp. 88–95, Dec. 2016.

[7] B. Shankar, M. E. Lagunas, S. Chatzinotas, and B. Ottersten, "Precoding for satellite communications: Why, how and what next?," *IEEE Commun. Lett.*, vol. 25, no. 8, pp. 2453–2457, Aug. 2021.

[8] S. M. Ivari, M. Caus, M. A. Vazquez, M. R. Soleymani, Y. R. Shayan, and A. I. Perez-Neira, "Precoding and scheduling in multibeam multicast NOMA based satellite communication systems," in *Proc. IEEE Int. Conf. Commun. Workshops*, 2021, pp. 1–6.

[9] A. Guidotti and A. Vanelli-Coralli, "Design trade-off analysis of precoding multi-beam satellite communication systems," in *Proc. IEEE Aerosp. Conf.*, 2021, pp. 1–12.

[10] G. Taricco and A. Ginesi, "Precoding for flexible high throughput satellites: Hot-spot scenario," *IEEE Trans. Broadcast.*, vol. 65, no. 1, pp. 65–72, Mar. 2019.

[11] A. m. Al-Nimrat, M. Smadi, O. A. Saraereh, and I. Khan, "An efficient channel estimation scheme for mmWave massive MIMO systems," in *Proc. IEEE Int. Conf. Commun., Netw. Satell.*, 2019, pp. 1–8.

[12] ETSI. "Technical specification - 5G; NR; physical channels and modulation (3GPP TS 38.211 version 16.3.0 Release 15)," Tech. Rep. ETSI TS 138 211, 2020.

[13] A. Li et al., "A tutorial on interference exploitation via symbol-level precoding: Overview, state of the art and future directions," *IEEE Commun. Surv. Tuts.*, vol. 22, no. 2, pp. 796–839, Apr.–Jun. 2020.

[14] Y. Liu and W.-K. Ma, "Symbol-level precoding is symbol-perturbed ZF when energy efficiency is sought," in *Proc. IEEE Int. Conf. Acoust., Speech Signal Process.*, 2018, pp. 3869–3873.

[15] J. W. Lee and C. G. Kang, "Performance of MMSE-based symbol-level precoding in multi-user MISO system," in *Proc. 25th Asia-Pacific Conf. Commun.*, 2019, pp. 347–351.

[16] A. Li and C. Masouros, "Interference exploitation precoding made practical: Optimal closed-form solutions for PSK modulations," *IEEE Trans. Wireless Commun.*, vol. 17, no. 11, pp. 7661–7676, 2018.

[17] A. Li, C. Masouros, B. Vucetic, Y. Li, and A. L. Swindlehurst, "Interference exploitation precoding for multi-level modulations: Closed-form solutions," *IEEE Trans. Commun.*, vol. 69, no. 1, pp. 291–308, Jan. 2021.

[18] A. Haqiqatnejad, F. Kayhan, and B. Ottersten, "Power minimizer symbol-level precoding: A closed-form suboptimal solution," *IEEE Signal Process. Lett.*, vol. 25, no. 11, pp. 1730–1734, Nov. 2018.

[19] A. Haqiqatnejad, F. Kayhan, and B. Ottersten, "An approximate solution for symbol-level multiuser precoding using support recovery," in *Proc. IEEE Workshop Signal Process. Adv. Wireless Commun.*, 2019, pp. 1–5.

[20] J. Krivochiza, J. Merlano-Duncan, S. Andrenacci, S. Chatzinotas, and B. Ottersten, "Closed-form solution for computationally efficient symbol-level precoding," in *Proc. IEEE Glob. Commun. Conf.*, 2018, pp. 1–6.

[21] M. Á. Díaz, N. Courville, C. Mosquera, G. Liva, and G. E. Corazza, "Non-linear interference mitigation for broadband multimedia satellite systems," in *Proc. Int. Workshop Satell. Space Commun.*, 2007, pp. 61–65.

[22] L. Martinez Marrero, J. C. Merlano Duncan, J. Querol, S. Chatzinotas, A. J. Camps Carmona, and B. Ottersten, "Effects of multiple oscillator phase noise in precoding performance," in *Proc. Int. Commun. Satell. Syst. Conf.*, Okinawa, Japan, 2019, pp. 1–7. [Online]. Available: http://orbilu.uni.lu/handle/10993/40625

[23] J. Guerreiro, R. Dinis, and P. Montezuma, "Analytical performance evaluation of precoding techniques for nonlinear massive MIMO systems with channel estimation errors," *IEEE Trans. Commun.*, vol. 66, no. 4, pp. 1440–1451, Apr. 2018.

[24] R. Krishnan et al., "Linear massive MIMO precoders in the presence of phase noise - A large-scale analysis," *IEEE Trans. Veh. Technol.*, vol. 65, no. 5, pp. 3057–3071, May 2016.

[25] O. Raeesi, A. Gokceoglu, Y. Zou, E. Björnson, and M. Valkama, "Performance analysis of multi-user massive MIMO downlink under channel non-reciprocity and imperfect CSI," *IEEE Trans. Commun.*, vol. 66, no. 6, pp. 2456–2471, Jun. 2018.

[26] T. Kebede, Y. Wondie, and J. Steinbrunn, "Massive MIMO linear precoding techniques performance assessment," in *Proc. Int. Symp. Netw., Comput. Commun.*, 2021, pp. 1–8,.

[27] V. A. Beulah and S. Markkandan, "Performance analysis of precoding techniques for massive MU-MIMO systems," in *Proc. Int. Conf. Innov. Inf., Embedded Commun. Syst.*, 2015, pp. 1–5,.

[28] A. Guidotti, C. Amatetti, F. Arnal, B. Chamaillard, and A. Vanelli-Coralli, "Location-assisted precoding in 5G LEO systems: Architectures and performances," in *Proc. Joint Eur. Conf. Netw. Commun. 6G Summit*, 2022, pp. 154–159.

[29] B. R. Elbert, *Introduction to Satellite Communication* (Artech House Space Applications Series). Norwood, MA, USA: Artech House, 2008.

[30] L. M. Marrero, J. C. M. Duncan, J. Querol, S. Chatzinotas, A. Camps, and B. Ottersten, "A design strategy for phase synchronization in Precoding-enabled DVB-S2X user terminals," in *Proc. IEEE Int. Conf. Commun.*, 2021, pp. 1–7,.

[31] E. Bjornson, M. Bengtsson, and B. Ottersten, "Optimal multiuser transmit beamforming: A difficult problem with a simple solution structure[Lecture Notes]," *IEEE Signal Process. Mag.*, vol. 31, no. 4, pp. 142–148, Jul. 2014.

[32] N. Fatema, G. Hua, Y. Xiang, D. Peng, and I. Natgunanathan, "Massive MIMO linear precoding: A survey," *IEEE Syst. J.*, vol. 12, no. 4, pp. 3920–3931, Dec. 2018.

[33] C. Masouros and G. Zheng, "Exploiting known interference as green signal power for downlink beamforming optimization," *IEEE Trans. Signal Process.*, vol. 63, no. 14, pp. 3628–3640, Jul. 2015.

[34] M. Alodeh, S. Chatzinotas, and B. Ottersten, "Constructive multiuser interference in symbol level precoding for the MISO downlink channel," *IEEE Trans. Signal Process.*, vol. 63, no. 9, pp. 2239–2252, May 2015.

[35] A. Haqiqatnejad, F. Kayhan, and B. Ottersten, "Constructive interference for generic constellations," *IEEE Signal Process. Lett.*, vol. 25, no. 4, pp. 586–590, Apr. 2018.

[36] A. Haqiqatnejad, F. Kayhan, and Ottersten, "Symbol-level precoding design based on distance preserving constructive interference regions," *IEEE Trans. Signal Process.*, vol. 66, no. 22, pp. 5817–5832, Nov. 2018.

[37] M. Slawski and M. Hein, "Non-negative least squares for high-dimensional linear models: Consistency and sparse recovery without regularization," *Electron. J. Statist.*, vol. 7, pp. 7661–7676, 2013.

[38] A. Haqiqatnejad, F. Kayhan, and B. Ottersten, "Energy-efficient hybrid symbol-level precoding for large-scale mmWave multiuser MIMO systems," *IEEE Trans. Commun.*, vol. 69, no. 5, pp. 3119–3134, May 2021.

[39] L. Galleani, "A tutorial on the two-state model of the atomic clock noise," *Metrologia*, vol. 45, no. 6, 2008, Art. no. S175.

LIZ MARTINEZ MARRERO (Student Member, IEEE) was born in Havana, Cuba, in 1989. She received the M.Sc. degree in telecommunications and Telematics from the Technological University of Havana (CUJAE), Havana, Cuba, in 2018. She is currently working toward the Ph.D. degree as a Doctoral Researcher with the Interdisciplinary Centre for Security, Reliability, and Trust of the University of Luxembourg, Esch-sur-Alzette, Luxembourg. Her research interests include digital signal processing for wireless communications, focusing on the physical layer, satellite communications, and carrier synchronization for distributed systems. She was the recipient of the Best Student Paper Award during the 37th International Communications Satellite Systems Conference (ICSSC2019).

ALIREZA HAQIQATNEJAD (Member, IEEE) received the B.Sc. degree in electrical engineering from the Isfahan University of Technology, Isfahan, Iran, in 2012, the M.Sc. degree in telecommunications engineering from the University of Isfahan in 2015, and the Ph.D. degree in computer science from the Interdisciplinary Centre for Security, Reliability, and Trust (SnT), University of Luxembourg, Esch-sur-Alzette, Luxembourg, in 2021. He is currently a Research Associate (Postdoctoral Researcher) with SnT, the University of Luxembourg. His research interests include signal processing and optimization for wireless and satellite communication systems, interference mitigation in multiuser MIMO channels, and advanced precoding techniques for future generation wireless communications.

JUAN C. MERLANO DUNCAN (Senior Member, IEEE) received the Diploma degree in electrical engineering from the Universidad del Norte, Barranquilla, Colombia, in 2004, the M.Sc. and Ph.D. Diploma (Cum Laude) degrees from the Universitat Politècnica de Catalunya (UPC), Barcelona, Spain, in 2009 and 2012, respectively. His research interests include wireless communications, remote sensing, distributed systems, frequency distribution and carrier synchronization systems, software-defined radios, and embedded systems. At UPC, he was responsible for the design and implementation of a radar system known as SABRINA, which was the first ground-based bistatic radar receiver using space-borne platforms, such as ERS-2, ENVISAT, and TerraSAR-X as opportunity transmitters (C and X bands). He was also the in charge of the implementation of a ground-based array of transmitters, which was able to monitor land subsidence with subwavelength precision. These two implementations involved FPGA design, embedded programming, and analog RF/Microwave design. In 2013, he joined the Institute National de la Recherche Scientifique, Montreal, Canada, as a Research Assistant with the design and implementation of cognitive radio networks employing software development and FPGA programming. He joined the University of Luxembourg, Esch-sur-Alzette, Luxembourg, where he currently works as a Research Scientist with the COMMLAB laboratory working on SDR implementation of satellite and terrestrial communication systems and passive remote sensing systems.

SYMEON CHATZINOTAS (Senior Member, IEEE) received the M.Eng. degree in telecommunications from the Aristotle University of Thessaloniki, Thessaloniki, Greece, in 2003, and the M.Sc. and Ph.D. degrees in electronic engineering from the University of Surrey, Guildford, U.K., in 2006 and 2009, respectively. He is currently a Full-Professor, and the Deputy Head of the SIGCOM Research Group, Interdisciplinary Centre for Security, Reliability, and Trust, University of Luxembourg, Esch-sur-Alzette, Luxembourg, and a Visiting Professor with the University of Parma, Parma, Italy. His research interests include multiuser information theory, cooperative/ cognitive communications, and wireless network optimization. He has been involved in numerous research and development projects with the Institute of Informatics Telecommunications, National Center for Scientific Research Demokritos, Institute of Telematics and Informatics, Center of Research and Technology Hellas, and Mobile Communications Research Group, Center of Communication Systems Research, University of Surrey. He has coauthored more than 400 technical papers in refereed international journals, conferences and scientific books. He was the co-recipient of the 2014 IEEE Distinguished Contributions to Satellite Communications Award, the CROWNCOM 2015 Best Paper Award, and the 2018 EURASIP JWCN Best Paper Award. He is currently on the Editorial Board of the IEEE OPEN JOURNAL OF VEHICULAR TECHNOLOGY and the *International Journal of Satellite Communications and Networking*.

BJÖRN OTTERSTEN (Fellow, IEEE) received the M.S. degree in electrical engineering and applied physics from Linköping University, Linköping, Sweden, in 1986, and the Ph.D. degree in electrical engineering from Stanford University, Stanford, CA, USA, in 1990. He has held research positions with the Department of Electrical Engineering, Linköping University, the Information Systems Laboratory, Stanford University, Stanford, CA, USA, the Katholieke Universiteit Leuven, Leuven, Belgium, and the University of Luxembourg, Esch-sur-Alzette, Luxembourg. From 1996 to 1997, he was the Director of Research with ArrayComm, Inc., a start-up in San Jose, CA, USA, based on his patented technology. In 1991, he was appointed Professor of signal processing with the Royal Institute of Technology (KTH), Stockholm, Sweden. He has been Head of the Department for Signals, Sensors, and Systems, KTH, and Dean of the School of Electrical Engineering, KTH. He is currently the Director for the Interdisciplinary Centre for Security, Reliability and Trust, University of Luxembourg. He was the recipient of the IEEE Signal Processing Society Technical Achievement Award, the EURASIP Group Technical Achievement Award, and the European Research Council advanced research grant twice. He has coauthored journal papers that received the IEEE Signal Processing Society Best Paper Award in 1993, 2001, 2006, 2013, and 2019, and nine IEEE conference papers Best Paper awards. He has been a board Member of IEEE Signal Processing Society, the Swedish Research Council and the boards of European Association For Signal Processing and the Swedish Foundation for Strategic Research. He has was the Editor in Chief of *EURASIP Signal Processing*, and acted on the Editorial Boards of IEEE TRANSACTIONS ON SIGNAL PROCESSING, *IEEE Signal Processing Magazine*, IEEE OPEN JOURNAL FOR SIGNAL PROCESSING, *EURASIP Journal of Advances in Signal Processing* and *Foundations and Trends in Signal Processing*. He is a Fellow of European Association For Signal Processing.